Eruptive history of the Late Quaternary Ciomadul (Csomád) volcano, East Carpathians, Part I: Timing of lava dome activity

P. Lahitte, S. Dibacto, D. Karátson, R. Gertisser, D. Veres

Eruptive history of the Late Quaternary Ciomadul (Csomád) volcano, East Carpathians, Part I: Timing of lava dome activity

Lahitte, P.[1], Dibacto, S.[1], Karátson, D.[2], Gertisser, R.[3], Veres, D.[4]

1: GEOPS, Univ. Paris-Sud, CNRS, Université Paris-Saclay, Rue du Belvédère, Bât. 504, 91405 Orsay, France

2: Eötvös University, Department of Physical Geography, H-1117 Budapest, Pázmány s. 1/C, Hungary

3: School of Geography, Geology and the Environment, Keele University, Keele, ST5 5BG, UK

4: Romanian Academy, Institute of Speleology, Clinicilor 5, 400006 Cluj-Napoca, Romania

Abstract

Located at the southern tip of the Intra-Carpathian Volcanic Range in Romania, and composed of a dozen dacitic lava domes, the Ciomadul (Csomád) volcanic complex is the youngest eruptive centre of the Carpatho-Pannonian Region. Whereas, in the last decade, the explosive history of Ciomadul since 50 ka has been well constrained by numerous studies, the chronology of the dome sequence still lacks robust chronological constraints and an extended analysis of all available data. Here, we apply a detailed K-Ar dating approach to refine the chronology of the lava dome eruptions, using the unspiked K-Ar Cassignol-Gillot technique. Our dating focused on the most voluminous central part of the lava dome complex. New eruption ages were determined following a strict separation (of 10 g) of groundmass from about 3 kg of unaltered sample rocks, thereby isolating material whose

cooling was contemporaneous with the eruption. The newly applied methodology, mainly consisting of a double full preparation, first at larger grain size (~ 0.4 mm) and then at < 100 µm, provides an appropriate procedure to separate suitable material to obtain the K-Ar age of the eruption, i.e. the sample's groundmass, in which there is no risk of the presence of older, inherited crystals. Our new geochronological data set gives an improved insight into the temporal construction of the Ciomadul volcanic complex, where (due to the method applied here) all ages are younger than those from previous studies that used whole-rock K-Ar ages. Our new results show that Ciomadul's volcanic activity began with the construction of the southeastern, peripheral domes from ca. 850 ka to 440 ka. After a ca. 250 ky long repose period, the activity resumed in the northern part at around 200 ka, with subsequent domes emplaced between 200 and 130 ka, aligned roughly north-south in the western-central part of the complex. Following a 30 ky long quiescence period, the eastern-central domes formed between 100 and 60 ka. In addition to the chronological history of lava dome volcanism, we also investigated the sequence of crystallisation of mineral phases present in the lavas with respect to the modification of eruption ages. Ages obtained on pure minerals (plagioclase, amphibole and biotite) are systematically older than those obtained on groundmass, showing that most of them formed up to 1.85 Myr before eruption in a long-lived, pre-Ciomadul magmatic system. Crystal size distributions (CSD) data support the age contrasts between juvenile groundmass and older inherited minerals. After injection of new magma and convective mixing with crystal clots, ascent of the resulting led to eruptions of material representing contrasting ages.

Keywords

43 K-Ar geochronology; groundmass; glomerocryst; excess argon; dacitic lava dome; crystal size
44 distributions; Quaternary volcanism

45 1 Introduction

46 Accurate, high-temporal resolution data on eruption ages are crucial to better constrain
47 the geochemical and petrological evolution of volcanic systems (e.g. Kersting and Arculus,
48 1994; Hildenbrand, 2004; Cadoux et al., 2005), as well as to infer hazard parameters such as
49 recurrence rates and repose periods (Marzocchi and Zaccarelli 2006; Damaschke et al. 2018;
50 Reyes-Guzman et al. 2018). The more accurately the volcanic activity is known, the better its
51 recurrence can be documented and its potential risk constrained (Turner et al. 2009). Such
52 ages also allow estimates of magma extrusion rates (Crisp 1984; Singer et al. 1997) and
53 detailed variations of eruption rates through time and space (Hora et al. 2007; Lahitte et al.
54 2012; Germa et al. 2015). Moreover, eruption ages help identify vent migration patterns
55 (Tanaka et al. 1986; Connor and Hill 1995; Condit and Connor 1996; Heizler et al. 1999) in
56 dispersed, monogenetic volcanic fields (Nemeth and Kereszturi 2015), and volcanic
57 processes, such as magma crystallisation, vesiculation and fragmentation, that are crucial for
58 eruption forecasting in both monogenetic (Kereszturi et al. 2017) and polygenetic volcanic
59 systems (Turner et al. 2011; Damaschke et al. 2018).

60 During its long-term evolution, the Miocene to Pleistocene volcanic activity of the Inner
61 Carpathian volcanic chain in the Carpathian-Pannonian Region (CPR; Fig. 1) shifted south-
62 eastward (Szabo et al. 1992; Lexa et al. 2010). This migration defined the Călimani-Gurghiu-
63 Harghita (CGH; Kelemen – Görgényi - Hargita) [1] range, East Carpathians, Romania (Pécskay et

[1] Official Romanian names, when mentioned at first, are followed by locally used Hungarian names (in brackets), which is helpful for the reader in finding the names on local maps

al. 1995, 2006). The youngest centre of the CPR, Ciomadul (Csomád) volcano, is located at the south-easternmost tip of the CGH range. It is a dacitic lava domes complex truncated by the well-preserved twin craters of St. Ana (Szent Anna) and Mohoş (Szakács and Seghedi 1995; Karátson et al. 2013). Ciomadul experienced a long-term eruptive history, producing a dozen lava domes emplaced during the last ca. 1 Myr over an area of 70 km² (Pécskay et al., 1995; Szakács et al., 2015). Its latest, mainly explosive, activity has been dated by radiocarbon and luminescence (OSL and post-IR IRSL) methods (Moriya et al. 1996; Vinkler et al. 2007; Harangi et al. 2010, 2015b; Karátson et al. 2013, 2016) around 32 ka. This has great significance for the regional, Late Quaternary tephrostratigraphy considering the areal distribution of these tephra which extend up to 350 km eastward (Karátson et al., 2016; Wulf et al., 2016). However, Ciomadul's whole volcanic history lacks a sufficiently constrained and reliable geochronological framework. Particularly, the recurrence time of the long-lasting dome-forming activity that preceded the explosive events is still poorly constrained. Previously obtained ages based on conventional K-Ar dating of the Ciomadul lava domes suffer from a lack of analytical accuracy (Pécskay et al. 1995; Szakács et al. 2015). An alternative approach, U-Th/He dating of zircon (Molnár et al. 2018), focused mostly on the onset of Ciomadul volcanism (around 1 Ma), without targeting the main area of the central dome complex.

Even Ciomadul have experienced a long dormant period to present , with no eruption in the past 10,000 years, it is susceptible to erupt again (Szakács et al. 2015). Indeed, magneto-telluric surveys suggest the presence of conductivity variations at various levels beneath Ciomadul that have been attributed to the presence of a partially molten magma body below the volcano (Harangi et al. 2015b). These authors interpreted these anomalies as a result of the presence of crystal-mush bodies containing about 5–15% melt fraction at

88 depths of 5-25 km and 30-40 km. These depths coincide with a low velocity seismic zone
89 located by crustal tomography (Popa et al. 2012).
90 This paper aims to constrain the main history of extrusive activity of Ciomadul, focusing
91 on the central dome complex and its peripheral lava domes. Due to the very young eruption
92 ages (in the 100 ka range), apart from the $^{40}Ar/^{39}Ar$ method, the unspiked Cassignol-Gillot
93 technique (Cassignol and Gillot, 1982; Gillot et al., 2006), which uses the K-Ar radioactive
94 chronometer, is arguably the most precise radiometric argon dating technique that can be
95 applied to Ca-rich volcanic rocks. . The advantage of this technique is that avoids recoil issues
96 of ^{39}Ar, ^{37}Ar, and ^{36}Ar in the reactor that may affect the $^{40}Ar/^{39}Ar$ technique. The method has
97 proven to be well-suited for dating recent up to Holocene lavas (Samper et al. 2009; Germa
98 et al. 2011b; Gertisser et al. 2012). In part 1 of this work, we use this method to obtain
99 precise eruption ages and constrain the geochemical evolution of the system. In part 2 we
100 use the results to also assess the geomorphological evolution and magma output rates that
101 characterized the evolution of Ciomadul's dome complex (Karátson et al., this volume). In
102 this way we build on previous work using high-precision Cassignol-Gillot K-Ar geochronology
103 at, for example, Basse-Terre (Samper et al. 2009), Martinique (Germa et al. 2011b, 2015) or
104 Merapi (Gertisser et al. 2012), in illustrating how a detailed geochronological framework can
105 support studies that also constrain magmatic evolution and time-space eruptive dynamism.

106 ## 2 Geological background

107 As volcanic activity migrated south-eastward along the CGH range during the Miocene
108 to Pleistocene (Pécskay et al., 1995, 2006), magma compositions evolved from normal calc-
109 alkaline to high-K calc-alkaline and shoshonitic (Szakács et al. 1993). This evolution was in
110 tandem with a decrease in magmatic output rates (Szakács and Seghedi 1995; Karátson and

Timár 2005). As decrease in the output rate is expressed by the progressive transition from large stratovolcanoes, occasionally with calderas, to smaller, mostly effusive cones and lava domes (Szakács and Seghedi, 1995; Karátson and Timár, 2005; Karátson et al., this volume).

Ciomadul volcano (Fig. 1) represents the best-preserved lava dome complex at the southernmost end of the CGH volcanic range. Its geological setting is presented in Szakács et al. (1993; 2015), Karátson et al. (2013; this volume), Harangi et al. (2015a) and Molnár et al. (2018). A dome complex is a special type of compound polygenetic volcano where an assemblage of nested lava domes, coulees (Blake 1990) and related pyroclastic and epiclastic volcanic rocks are spaced so closely in space and time that they are considered a polygenetic volcano rather than a group of monogenetic volcanoes (Lexa et al. 2010). Mostly high-K dacitic in composition, Ciomadul consists of domes resulting from extrusion of viscous magma and comprises the spatially and volumetrically most significant central dome in this system (Karátson et al., this volume). The system also includes the more isolated southeastern andesitic domes of Dealul Mare (Hegyes-tető) and the Puturosu (Büdös) Hills (Fig. 1), but these are not studied here. To the south, there are two other domes, which have andesitic to shoshonitic composition (Szakács et al., 2015). These latter domes, as well as the adjacent, western Pilişca (Piliske) stratovolcano in the South Harghita range are older than Ciomadul (Szakács et al., 2015; Molnár et al., 2018).

As already described elsewhere, such as at the Okataina Center in New Zeland's Taupo Volcanic Zone (Smith et al. 2004, 2005; Shane et al. 2007; Rubin et al. 2016), the magma batches of Ciomadul's dacites were probably produced as the result of reheating by intrusion(s) of hot mafic magma into a silicic reservoir (Kiss et al. 2014). In particular, crystallisation of amphibole has been related to the storage of a near-solidus silicic crystal mush body at 8 – 12 km depth (Kiss et al. 2014). The remobilization of silicic crystal mush can

provide a large amount of xenocrysts, which constitutes up to one third of the volume of the erupted silicic magma of some lava domes as observed, for instance, on Santorini or Montserrat (Zellmer et al. 2000, 2003). At Ciomadul, the role of these xenocrysts has yet to be shown and analysed. The xenocrysts, isolated or as part aggregates of crystals called glomerocrysts (or crystal clots), may have reached the surface with a part of the radiogenic argon ($^{40}Ar^{*}$) they had accumulated since their formation, making K-Ar dating of the dacitic domes challenging. Indeed, these xenocrysts are carriers of extraneous argon, which are prone to bias K-Ar ages (Dalrymple and Moore 1968; Stipp et al. 1969; Ozawa et al. 2006).

3 Petrology of the Ciomadul lava domes

Detailed petrology of the Ciomadul lava domes was already well established by previous studies ((Kiss et al. 2014; Harangi et al. 2015b; Szakács et al. 2015)). We here only highlight their main characteristics. Ciomadul lava dome rocks are mainly high-K calc-alkaline, poorly vesicular dacites. Mainly porphyritic, these rocks contain 20-35 vol% coarse crystals (most of them being xenocrystic, see below) commonly set in a fine-grained, light-grey groundmass. In order of relative abundance, these include plagioclase ($An_{85–30}$, 10-25 vol%), amphibole (5-13 vol%), biotite (1-4 vol%), orthopyroxene (1-2 vol%), and Fe-Ti oxides (1-2 vol%). Plagioclase occurs as euhedral laths up to 10 mm in size and often exhibits inclusions of green-brown biotite, euhedral amphibole, and sparse equant Fe-Ti oxide crystals. Euhedral crystals include mainly plagioclase, some exhibiting oscillatory zoning and sieve textures, and amphibole. Subhedral biotite is present as red-brown, pleochroic tabular laths up to 5 mm in length (Szakács et al. 2015). Red-brown hornblende (low-Al amphibole with thick breakdown rims) and pargasite (high-Al amphibole with thin reaction rims) are present as rounded, subhedral to anhedral crystals up to 10 mm in size (Kiss et al., 2014;

158 Harangi et al., 2015b), containing abundant inclusions of Fe-Ti oxides, plagioclase or biotite.
159 From thermobarometrical modelling, formation of amphiboles has been interpreted as
160 bimodal (Kiss et al., 2014); hornblende having formed at lower temperature (< 800°C) and
161 pargasite having formed at higher temperature (950°C).

162 The dome rocks contain abundant glomerocrysts or crystal clots, which are aggregates
163 of crystals. Importantly for dating, these glomerocrysts consist of remobilised crystals (> 1
164 mm and up to 15 mm in diameter, Fig. 2) with microdiorite textures, containing mainly
165 rounded and slightly altered plagioclase and amphibole, in addition to Fe-Ti oxides, apatite,
166 biotite and zircon. Such remobilised crystals are here referred to as xenocrysts, whereas the
167 term glomerocryst is used for an aggregate of xenocrysts remobilised from crystal mush. The
168 groundmass of the dome lavas contains plagioclase, hornblende, biotite with occasional
169 orthopyroxene, Fe-Ti oxide and glass.

170 # 4 Methods

171 ## 4.1 Applying the unspiked Cassignol–Gillot K-Ar technique

172 The unspiked Cassignol-Gillot technique allows the accurate detection of low
173 percentages of radiogenic ^{40}Ar (Quidelleur et al., 2001). It has been applied to the dating of
174 young (< 100 ka) volcanic events and successfully compared with other dating methods such
175 as ^{14}C, ^{36}Cl exposure and thermo-luminescence (Lahitte et al. 2001; Gillot et al. 2006; Germa
176 et al. 2010; Schimmelpfennig et al. 2011). The technique was also favourably compared with
177 the $^{40}Ar/^{39}Ar$ method and gave similar results when applied to groundmass samples (Coulie
178 et al. 2003; Calvert et al. 2006; Hildenbrand et al. 2014).

179 ### *4.1.1 The unspiked Cassignol–Gillot technique*

180 Independent K and Ar measurements were performed in the Laboratoire GEOPS
181 (GEOsciences Paris-Sud, Orsay, France). Following dissolution using a mixture of HF, nitric

and perchloric acids to destroy the silicate network, potassium (K) was measured by flame emission spectroscopy. Ar isotopic measurements were performed using a 180°-sector mass spectrometer (Cassignol and Gillot 1982; Gillot et al. 2006). This technique has a limit of detection for the radiogenic Ar content (^{40}Ar*) of only 0.1% of the total extracted argon (Quidelleur et al. 2001). Details of the Ar isotopic approach are given elsewhere (Cassignol and Gillot 1982; Gillot and Cornette 1986; Gillot et al. 2006) and are summarized in the Supplementary Material. To minimize the effect of mass-discrimination, the amount of radiogenic argon (%^{40}Ar*) was calculated from a direct comparison between the instrumental ^{40}Ar/^{36}Ar sample ratio and the instrumental ^{40}Ar/^{36}Ar atmospheric ratio at identical pressure. Unlike the conventional K-Ar technique, this direct quantification does not add a ^{38}Ar spike and is made possible by the very stable analytical conditions. Average relative uncertainties of the ^{40}Ar/^{36}Ar ratios and on the amount of radiogenic argon (%^{40}Ar*) are 0.045% and 1.533%, respectively. The technique relies on the assumption that all the measured ^{40}Ar* comes from the in-situ radioactive decay of ^{40}K.

4.1.2 Sample preparation

Extraneous argon, i.e. argon not generated by *in situ* decay of potassium, originates from inherited argon and excess argon, and may bias K-Ar ages (Dalrymple and Moore 1968; Stipp et al. 1969; Ozawa et al. 2006). Inherited argon consists of the contamination by older minerals incorporated into the juvenile magma before eruption, whereas excess argon is introduced from outside the system, commonly from fluid circulations (Kelley, 2002). Our sample preparation procedure (from fieldwork sampling to the sample separation) aims at isolating the groundmass from such a source of extraneous argon. Given the incompatible nature of argon, mineral/fluid and mineral/melt partition coefficients range from 0.01 to as low as 7×10^{-6}, and excess argon remains a relatively uncommon phenomenon (Kelley, 2002).

206 On the other hand, extraneous argon may result from the contamination by older country
207 rock (inherited argon in xenoliths), or by excess argon present either in inclusions of glass
208 within phenocrysts (Dalrymple and Moore 1968) or in hydrous fluid in the grain boundary
209 network (Kelley 2002). As K-Ar ages do not give spectra to check the presence of inherited
210 argon, dates may be erroneously too old due to such contamination sources. However,
211 accurate sampling, sample separation, and very strict selection of a narrow density range of
212 pure groundmass greatly minimizes the risk of contamination due to the presence of
213 extraneous argon.

214 *4.1.3 Sample selection*

215 During two field campaigns (in October 2015 and June 2016), 25 samples (about 3 kg-
216 weight each), were collected from Ciomadul's lava domes. The sample locations are shown
217 in Figure 1 with the UTM coordinates listed in Table 2. Some of the sampled domes were
218 assumed to be coeval with the late-stage (<50 ka) pyroclastic (fall and flow) deposits
219 (Harangi et al., 2010, 2015a, Karátson et al., 2013, 2016; Wulf et al., 2016). In the field, only
220 samples without visible obvious traces of alteration (calcite, zeolite, or any secondary
221 minerals) and fluid circulation were collected. An additional inspection of thin sections, and
222 checking the freshness of the groundmass, reduced the number of samples to be dated to
223 18, representing nine individual lava domes. The low loss-on-ignition (LOI) values (less than
224 1.6 wt%, Table 3) indicate that secondary weathering processes have not significantly
225 affected the selected samples. These criteria reduce the possible bias of K-Ar ages related to
226 K loss or gain via alteration.

227 *4.1.4 Sample separation*

228 One of the main issues in determining the eruption age of the xenocryst-bearing
229 lavas from the Ciomadul domes is to separate pure groundmass aliquots from numerous

xenocrysts and phenocrysts, which are potential carriers of extraneous argon. The probability of extraneous argon increases with the range of the groundmass density. Indeed aliquots having a large range of density may contain significant amounts of xenocryst and phenocryst fragments together with the groundmass. In our work, we lowered the relative density range to less than 0.05 (dimensionless quantity). To separate the groundmass as much as possible from inherited minerals, we applied a two-step procedure.

First, the whole-rock sample was crushed and sieved to the 250–500 μm size fraction and then ultrasonically washed in 10% nitric acid solution in order to remove any traces of alteration (clay, sulphur, carbonate, etc.) and hydrothermal products (zeolites, salt containing chlorine compounds, some of them being that isobar to argon isotopes). Finally, the sample was rinsed with water, ethanol and acetone, and ca. 200 g clean material was obtained. Neither HF nor HCl acid were used during sample cleaning in order to avoid 36 mass isobaric contamination (by HCl) that could bias the ^{36}Ar detection or induce dissolving and loss of K (HF and HCl) as was observed in the study of Balogh et al. (2010). Groundmass aliquots were separated by means of heavy liquids (bromoform progressively diluted in ethanol) and, if necessary, by magnetic separation (Gillot et al. 1992). This procedure was efficient in separating the mixed grains of biotite/groundmass or amphibole/groundmass from the pure groundmass, although, in some cases, it was not possible to eliminate the mixed plagioclase/groundmass grains.

This first preparation step was followed by additional crushing to the 62.5-125 μm size fraction (Fig. 3b). After cleaning, a second density separation was performed to isolate the groundmass fraction (Fig. 3c) from the remaining plagioclase crystals (Fig. 3d). Following the density separation, magnetic separation and handpicking were performed to guarantee the absence of plagioclases in the aliquots to be dated.

Pure phenocrysts and xenocryts (K-feldspar, plagioclase, biotite and amphibole) were separated from the 250-500 µm fraction in an attempt to estimate the contribution of inherited argon in whole-rock dating. We also separated plagioclase microphenocrysts from samples 16CIO01 and 16CIO04 as their groundmass was slightly altered.

4.2 Crystal size distribution analysis

In order to highlight the petrographical properties of the Ciomadul dacitic lavas and, and determine its impact on the ideal fraction for K-Ar dating, crystal size distribution (CSD) analyses were obtained on representative samples, following standard methods (Higgins 1996). High-resolution photomicrographs were taken and digitally merged together to create single large thin-section images. These images (6400 × 4800 pixels) were imported into ImageJ software, where contrast and brightness were adjusted to highlight crystal boundaries. For each crystal population, including plagioclase (selected by white and/or bright zones) and mafic crystals (amphibole and biotite, orange to dark brown zones), colour histogram analyses and thresholding were applied to outline crystals. Small crystals (< 10 pixels) were removed from these binary images. Best-fit ellipses were applied to determine long- and short-axis measurements. Mean crystal aspect ratios were calculated using the CSDSlice methodology (Morgan and Jerram 2006). For all grain categories, the number of measurements was at least 10 times higher than the minimum recommended (Mock and Jerram 2005; Morgan and Jerram 2006). Intersection lengths were converted to 3-D CSDs, using the CSDCorrections 1.6 software (Higgins 1996, 2002, 2006). L_{max} is calculated by averaging the four largest crystals within each identified population. The lower limit of the CSD was 0.010 mm (which is not necessarily the smallest crystal in the rock). Samples were classified as massive and approximate crystal roundnesses of 0.3 for plagioclase and 0.6 for

277 mafic crystals (on a scale of zero, angular, to one, spherical) were used. Logarithmic length
278 intervals were used, with each bin $10^{0.2}$ times the size of the previous bin. Bins with less than
279 three crystals were removed from the CSD analysis. Where CSD slopes were curved or
280 kinked, individual segments were interpreted using least squares regression.

281 4.3 Petrographical and geochemical analyses

282 To highlight the importance of the main mineral phases, a petrographical analysis was
283 performed in order to estimate the relative proportion of the main phenocrysts (plagioclase,
284 biotite, and amphibole), xenocrysts, glomerocrysts and groundmass. Major-element whole-
285 rock analyses were also performed on the newly dated lava rock samples by ICP-AES to
286 assess the geochemical evolution through time. The samples were analysed at Bureau
287 Veritas Minerals, Vancouver, Canada, following standard sample preparation and analytical
288 techniques.

289 # 5 Results

290 5.1 Crystal size distribution analysis and justification of the groundmass separation process

291 Crystal size distribution data based on the major axis of the fitting ellipsoid and
292 results are presented in Table 1. Almost all samples (black curves in Fig. 4a) show CSD plots
293 for both plagioclase and mafic mineral phases that exhibit kinked profiles, allowing each to
294 be divided into two individual segments. On the other hand, sample 16ClO08 differs with its
295 much more linear CSD profile (coloured curves in Fig. 4a), particularly for the mafic minerals.
296 A downturn in the smallest crystal sizes can appear either from real population proportions
297 or from analytical bias (Higgins 1996, 2002). Considered as representing a left-hand
298 truncation effect, these bins were removed from analyses.

299 Plots for plagioclase show the most prominent kinked CSDs (black curve, Fig. 4b).
300 Each curve can be divided into two distinctive segments, defined by sizes <0.125 and > 1
301 mm. Volumetric plagioclase proportions range from 29.5 to 38.0 vol% and maximum length
302 (L_{max} in Table 1) from 2.93 to 4.79 mm. Average characteristic length values, defined as the
303 opposite of the inverse of the slope (Marsh 1988), are around 0.02 mm for the smaller
304 populations and range from 0.65 to 2.12 mm for the larger ones.

305 Mafic mineral (biotite) CSDs show concave-upward patterns that are smoother than
306 those for plagioclase (grey curve, Fig. 4c) but kinked enough to divide trends into two slopes
307 (<0.125 and > 1 mm). Volumetric mafic mineral proportions range from 7.9 to 12.3 vol% and
308 L_{max} from 1.39 to 2.08 mm. Average characteristic length values range from 0.016 to 0.025
309 mm for the smaller mafic populations and from 0.32 to 0.50 mm for the larger ones.

310 Using the method of Marsh (1988), and from the growth rates of plagioclase
311 microphenocrysts estimated at around 1×10^{-10} mm s^{-1} (Higgins and Roberge 2007),
312 residence times for these populations are around six years. Such delay cannot be related to
313 the magma ascent (estimated at 12 days by Kiss et al., 2014), but to the magma storage
314 preceding eruption (Kiss et al., 2014; Harangi et al., 2015b).

315 CSD plots do not take into account more than 50 % of the total crystal volume (grey
316 in Fig 4A insets). This is the population corresponding to grains smaller than 0.010 mm, and
317 constitutes the microlitic groundmass. This population represents material that crystallised
318 during the eruption.

319 As the microlitic fraction and microphenocrystic populations not contain pre-eruption
320 inherited argon that may bias results, it represents the ideal fraction for eruption age
321 determination. We hereafter refer to this population as groundmass. The 0.125 – 1 mm

fraction corresponds to the juvenile magma groundmass and the smaller phenocrysts, possibly inherited as xenocrysts. As a result, this population is not suitable for determining an eruption age. The > 1 mm fraction is mostly made up of pre-eruptive and, possibly, inherited-argon-rich minerals. As crushing would reduce the larger minerals into grains having the same size and almost the same density as the smaller minerals, simply crushing and separating them in a single-step procedure is not suitable. Groundmass aliquots were thus obtained during the two-step procedure described above (see also Fig. 3), with each separation step contributing to the maximum possible purification of the originally <0.125 mm fraction by removing grains considered to have originated from phenocrysts or glomerocrysts, i.e. from any crystals initially larger than 0.125 mm.

5.2 K-Ar ages

K-Ar ages are reported in Table 2, with all uncertainties quoted at the one-sigma (1σ) level. Age calculations are based on the ^{40}K abundance and decay constants recommendedby Steiger and Jager (1977). The argon content is calculated from two independent measurements. As a higher abundance of radiogenic $^{40}Ar^*$ means a lower uncertainty on the age, the average age and its 1-σ uncertainty have been calculated by weighting each independent age measurement with its amount of radiogenic $^{40}Ar^*$. Percentages of $^{40}Ar^*$ range from 1.03% to 34.3 vol%, with respective relative uncertainties between 6.48% and 0.27%. Relative errors of the ages are between 12.6% and 1.44%, the latter value being near the limit of our method set at 1.42% for a 100% radiogenic sample, i.e. when only the relative uncertainties on K-content (1%) and argon calibration (1%) affect the result. With the exception of sample 16CIO04, all Ar analyses were successfully duplicated at the 1-σ level (Table 2). The poor reproducibility of sample 16CIO04 may reflect

grain heterogeneity within the sample. In this case, the uncertainty of the age was calculated as the standard deviation of the duplicated age measurements.

Even if our strict selection effectively removed phenocrysts, glomerocrysts and their fluid inclusions, greatly minimizing the risk of biasing ages by excess argon, we have to consider that the elimination of excess argon might not have been perfect. Such cases would induce eruption ages that are slightly younger than our results.

5.2.1 South-eastern and northern domes

Three new K-Ar ages constrain the emplacement time of the peripheral domes of the Ciomadul area (Table 2, Fig. 1 and Fig. 5) in addition to the somewhat older Dealul Mare. The radiogenic argon content ($^{40}Ar^*$) of the dated samples varies from 4 to 35 vol%, this latter value being related to the exceptional freshness of the sample, yielding very low atmospheric contamination. The groundmass K content is homogenous, from 3.23 to 3.59 wt%.

The two south-eastern peripheral domes of Muntele Puturosu (Büdös Hill) and Balvanyos (Bálványos Hill) represent relicts of apparently heavily eroded domes that cut through the Cretaceous flysch (Szakács et al., 1993, 2015). Muntele Puturosu was dated at 704 ± 18 ka (16CIO08). The Balvanyos dome, which is the south-easternmost volcanic extrusion of the Ciomadul area (Fig. 1), is dated at 641 ± 9 ka (16CIO07) and 440 ± 12 ka (16CIO06). Based on the more proximal position of 16CIO07 the 641 ka age may better constrain the emplacement age of the Balvanyos dome, and the younger sample could be linked to another, nearby eruption source no longer morphologically visible. Due to the small error even at the 2σ level, it can be concluded that the two samples are from successive, adjacent eruptions separated by a long time gap.

In the north, the groundmass separated from the sample collected from the Haramul Mic (Kis-Haram) dome (16CIO01) shows very high atmospheric contamination. Therefore, no trustworthy age could be obtained on the groundmass. Instead, plagioclase microphenocrysts, which crystallized shortly before eruption were processed, giving an age of 245 ± 24 ka. However, due to presence of glomerocrysts, the probability that the aliquots of plagioclase microphenocrysts contain inherited grains is not zero. As a consequence, the K-Ar age has to be considered a maximum value. Because Haramul Mic is the oldest part of the main dome complex, this age implies that most of the extrusive dome activity of Ciomadul was constrained within the past 250 ky.

5.2.2 Western-central part of the dome complex

The most important results of our work are related to the western-central main part of the dome complex, which represents the largest volume of Ciomadul (Karátson et al., this volume). Of these domes, only Haramul Mare (Nagy-Haram), Dealul Cetăţii (Vár-tető), Dealul Taca (Fáca) and Piscul Pietros (Köves Ponk) have been dated by applying the conventional K-Ar technique (Pécskay et al. 1992, 1995; Szakács et al. 2015). In addition, Piscul Pietros was also dated by the U-Th/He method (Harangi et al. 2015a), whereas Dealul Cetăţii (Vár-tető) and Haramul Lerbos (Fű-Haram) were dated using uncorrected U-Th/He measurements (Karátson et al. 2013), only providing age ranges.

The obtained ages define a 50 ky time span from about 184 ka to 133 ka (Table 2, Fig. 1 and Fig. 5), showing that the majority of the Ciomadul domes were formed in a relatively short time interval. The K-content varies from 1.39 wt% (on plagioclase microphenocrysts) to 3.72 wt% (groundmass), whereas radiogenic argon contents (^{40}Ar*) range from 1.2 to 4.4 vol%, inducing relative uncertainties between 3 and 14%. The Dealul Cetăţii (Vár-tető) dome in the north has been dated at 184 ± 5 ka (sample 15CIO01), whereas the Vârful Comlos

(Komlós-tető) dome (sample 16CIO02) yielded an age of 144 ± 4 ka. Adjacent to Vârful Comlos, the dome of Ciomadul Mare (sample 16CIO04) represents the northern rim of the twin-craters of St. Ana and Mohoş, and may morphologically correspond to an older, larger explosion crater (Karátson et al. 2013; Szakács et al. 2015) created during the early Mohoş explosive eruptions. To minimize risk of contamination by gas released during the last explosive phase from the younger craters, and because the St. Ana crater area is still experiencing gas emanation, the material retained to date this dome consisted of plagioclase microphenocrysts. These were separated by the two-step procedure from the 40 – 80 μm grain size fraction obtained after crushing the 80 - 160 μm groundmass fraction. The very small grain size used in both steps allowed minimization of the traces of inherited minerals. The extracted plagioclase microlite fraction, which is expected to be contemporaneous with the eruption, provided an age of 133 ± 18 ka (Table 2), indistinguishable from the Vârful Comlos data, even at 1σ level.

5.2.3 Eastern-central part of the dome complex

After a quiescence lasting tens of thousands of years, volcanic activity resumed at around 100 ka to form the eastern-central domes (Fig. 1). The Haramul Mare dome (sample 15CIO09), has been dated at 96 ± 2 ka (Table 2). At the southern rim of the Mohoş crater, a rock sampled on the active face of a quarry offered access to a fresh sample of the Piscul Pietros (Köves Ponk) dome, which is morphologically truncated by the Mohoş crater. It has been dated at 60 ± 5 ka (sample 16CIO09, Table 2).

5.3 Geochemistry of the lava domes

Representative chemical analyses of the dated samples are given in Table 3. Concentrations of SiO_2 for the Ciomadul lava domes range between 62.8 and 68.4 wt%, and belong to the high-K calc-alkaline (HKCA) series. There is a dacitic composition for all but two

samples of the Balvanyos dome (16CIO06 and 16CIO07), the latter straddling the boundary with the high-K andesite field (Fig. 6a). We note that the southern Dealul Mare dome, not studied here, also falls in this latter andesite field (Szakács et al., 2015).

Major element contents (using SiO_2 as a differentiation index; Fig. 6b) show that MgO, CaO, Al_2O_3, MnO, Fe_2O_3, P_2O_5 and TiO_2 decrease with SiO_2, whereas K_2O slightly increases; as does Na_2O but with a more scattered distribution. These evolutionary trends are consistent with fractional crystallization of plagioclase, amphibole, pyroxene, biotite and Ti-Fe oxides. Specifically, the decreasing trends of CaO and Al_2O_3 as SiO_2 increases, for all samples but 16CIO08, are explained by predominantly plagioclase fractionation.

6 Discussion

6.1 Timing of lava dome activity

Our new K-Ar ages for the extrusive products of the Ciomadul lava dome complex allow better constraints on its dynamism. In particular, they reduce the age range previously suggested by Pécskay et al. (1995) and Szakács et al. (2015), showing that the mainly extrusive, dome-building activity occurred in two main stages and is younger than 1 Ma.

Our derived ages indicate that two stages can be distinguished in the construction of the Ciomadul system. The first stage (Table 2) produced the south-eastern peripheral domes of Muntele Puturosu and Balvanyos (Figure 1). In addition to the somewhat older Dealul Mare (Szakács et al. 2015; Molnár et al. 2018), the duration of this stage is constrained between around 850 and 440 ka. The second, and volumetrically most significant, stage of Ciomadul, began around 200 ka with the Haramul Mic dome-forming eruption. This stage built the northern and central portions of the dome complex. In turn, the main lava domes that form this second stage can be divided into two phases, an older phase between 200 and

130 ka and a younger phase beginning around 100 ka. Within the second phase, the 60 ka age of Piscul Pietros roughly coincides with the onset of the late-stage explosive eruptions (Harangi et al. 2015a; Karátson et al. 2016). Overall, the activity of the Ciomadul lava-dome complex is aligned approximately north-south, sub-parallel to a local fault (Matenco et al. 2007). This suggests a tectonic control on magma extrusion which was characterized by two stages, separated by a long repose of ca. 440-200 ka. Dome eruptions over the main eruptive stage of Ciomadul (< 200 ka) point to a recurrence time of ca. 30 ka. Such an interval is in the same order of magnitude as the age of the latest volcanic event (Karátson et al., 2016), confirming the dormant (i.e. not extinct) status of the volcano as also suggested by fumarole activity (Vaselli et al. 2002; Kis et al. 2017), seismic tomography (Popa et al. 2012), and magnetotelluric surveys (Kiss et al. 2014; Harangi et al. 2015b).

6.2 Comparison with previous radiometric results

The issue of obtaining radiometric ages from whole-rock has been demonstrated elsewhere as possibly inducing biased results (Hofmann et al. 2000; Samper et al. 2007; Germa et al. 2011a). For instance, $^{40}Ar/^{39}Ar$ dating of lava domes on Montserrat yielded an age of 223 ± 7 ka using whole rock, whereas groundmass measurements produced an age of 155 ± 5 ka (Harford et al. 2002). The same study on the active dome obtained a surprisingly old age of 426 ± 95 ka on pure plagioclase and only 21 ± 22 ka on the groundmass fraction. This bias is particularly significant for young samples where any contamination effect would be magnified proportionally to the small amount of in-grown radiogenic Ar. In contrast to various crystal phases, the groundmass is the last phase to crystallize when the lava cools upon eruption. It is thus enriched in incompatible elements, including potassium, and in

461 elements which are in equilibrium with the atmosphere. Hence the initial argon isotopic
462 ratios in the groundmass are atmospheric, and are devoid of radiogenic argon ($^{40}Ar^*$).

463 Szakács et al. (2015) excluded the possibility of overestimated ages as they considered
464 quartz phenocrysts as the most likely source of excess argon, which are very uncommon in
465 the Ciomadul lavas (Kiss et al., 2014). However, as seen in Table 4 and Fig. 4, our groundmass
466 ages contrast with those obtained from whole rock analyses by applying the conventional K-
467 Ar method (Pécskay et al. 1995; Szakács et al. 2015). Only one sample (16CIO08, M. Puturosu
468 dome) has an age (704 ± 18 ka); compatible at 1-σ level with that obtained from whole rock
469 by the conventional K-Ar technique (710 ± 40 ka, Table 4). For the remaining samples,
470 considering the 2-σ level, only two out of the seven ages match, but these agreements are
471 mostly due to the large uncertainties on conventional K-Ar results (Fig. 5; Table 4).

472 Biotite from the Piscul Pietros dome, which was dated by both techniques, gave
473 comparable ages of 290 ± 110 ka by conventional K-Ar (Szakács et al. 2015) and 196 ± 4 ka by
474 the unspiked Cassignol-Gillot technique (this work); again the overlap of the ranges is only
475 due to the very large error of the former. On the other hand, neither of these two ages are
476 consistent with the age of 560 ± 110 ka initially proposed by Pécskay et al. (1992).

477 Our groundmass dating of the Balvanyos dome, the south-easternmost Ciomadul
478 dome (Fig. 1), yielded ages of 641 ± 9 ka (16CIO07) and 440 ± 12 ka (16CIO06), in contrast to
479 previous ages of 920 ± 180 ka and 1020 ± 150 ka obtained by whole-rock K-Ar dating
480 (Pécskay et al. 1995). Again, the minimal overlap (at 2σ) with the age obtained by the
481 unspiked Cassignol-Gillot technique is only due to the very large error. Consequently, it is
482 likely that these ages would not be coeval, if measured with the same range of uncertainties.
483 It thus involves a possible shift toward older ages for the whole-rock K-Ar measurements,
484 mostly induced by inherited argon.

485 One of the most controversial ages of Ciomadul was assigned to the northernmost
486 dome, Haramul Mic (Kis-Haram), with an unpublished K-Ar age of 0.85 Ma (without reported
487 uncertainties by Casta (1980), quoted in Szakács et al. 2015). Karátson et al. (2013) argued
488 that the recent "pancake" shape of the dome (which is in contrast to other, high and steep-
489 sided Peléan domes and coulées of Ciomadul) is not due to the old age, but simply reflects
490 the original flat dome shape. Indeed, we dated this dome at 245 ± 24 ka using plagioclase
491 microphenocrysts, which provides a maximum age. Szakács et al. (2015) also reported a K-Ar
492 age of 210 ± 50 ka obtained from a block 2 km west of the dome. In agreement with this
493 date, our dating confirms that, after at least a ca. 250 ky-long quiescence, extrusive activity
494 resumed at Haramul Mic less than 250 ka ago.
495 The systematic offset between groundmass and whole rock ages can be related to an
496 extraneous ^{40}Ar component in the whole rock measurement, which comes from the
497 inclusion of xenocrystic minerals. To evaluate the effect of extraneous ^{40}Ar on age results,
498 we conducted a component analysis on a thin section of sample 15CIO01 (Fig. 3a), whose
499 groundmass was dated at 184 ± 5 ka. Our aim was to calculate a whole-rock age by
500 combining ages of the groundmass and the plagioclase fraction (the two dominant phases)
501 with respect to their proportions in the sample. For the calculation, the thin section image
502 was converted to a black and white image by setting a threshold. Below a value of 20% on
503 the gray scale pixel is converted in black, otherwise is converted in write. This allows us to
504 distinguish plagioclase (in white in Fig. 7a) from groundmass (in black). Because of the
505 sample grain size (200 µm), the composition was next simulated by averaging the tone of
506 each 200 µm-wide subset (i.e. 40 pixel-wide square zones on the image). The composition
507 was then defined on the grey scale, from a material of pure plagioclase (100% on grey scale,
508 i.e. white on Fig. 7a), to one fully composed of groundmass (0% on grey scale, i.e. black on

509 Fig. 7a), including mixed material defined by an intermediate tone on grey scale (Fig. 7a). In
510 order to highlight the composition of each grain, a colour map is also proposed (Fig. 7b).
511 Pure plagioclase and pure groundmass grains are coloured in yellow and blue, respectively.
512 Mixed grains are illustrated by variation of red lightness: black for grain having a composition
513 almost similar of a groundmass grain, red for the perfectly intermediate composition (50%
514 groundmass - 50% plagioclase), white for grain having a composition almost similar of a
515 plagioclase grain (Fig. 7b). The age of each grain population was then modelled by
516 considering its plagioclase/groundmass ratio (dotted black curve in Fig. 7c). The thin section
517 reveals a composition of about 11 vol% of pure plagioclase dated at 1.1 Ma (Table 5), 60
518 vol% of pure groundmass dated at 184 ka (Table 1), and 29 vol% of mixed grains with mixed
519 ages (Fig. 7c). Applying the mixing theory to our multiphase and multi-age sample (Boven et
520 al. 2001), the whole rock age can be constrained by weighting each grain population age by
521 its proportion of the total:

522 $$A = (\Sigma\, a_i \times p_i \times K_i)/ (\Sigma\, p_i \times K_i) \qquad \text{(Eq. 1)}$$

523 where a_i, p_i and K_i are ages (right Y-axis values in Fig. 7c), proportions, and K-contents of
524 each grain population i, respectively. Such a calculation using a whole rock age model gives
525 320 ± 8 ka, 74% older than the groundmass age of 184 ± 5 ka, and in agreement with the 400
526 ± 160 ka age previously obtained from whole rock data for the same dome (Szakács et al.
527 2015). The whole rock model age shows the effect of only superficially removing the
528 inherited xenocrysts from groundmass, as performed in the previous K-Ar studies.

529 A relationship between the volume percentages of glomerocrysts and inherited
530 radiogenic argon was also assessed (Table 4). To apply this, the volume percentage of
531 glomerocrysts is obtained from thin section analysis, and a proxy of inherited radiogenic
532 argon is calculated as follows:

$$^{wr}Ar_i = (^{wr}Age - ^{gm}Age) / ^{wr}A \quad \text{(Eq. 2)}$$

where $^{wr}Ar_i$ is the percentage of radiogenic argon assumed to have originated from inherited minerals, and ^{wr}Age and ^{gm}Age are the ages obtained from whole rock and groundmass analyses, respectively. All samples dated by both techniques were considered. The sample with no glomerocrysts (16CIO08, M. Puturosu dome) is the only one that does not display inherited argon as the whole rock and groundmass ages are coeval. It is also the sample where the CSD plot presents the most linear relationship. This can be taken as a sign of a single crystal population, or a minimal proportion of inherited crystals (coloured curves in Fig. 4a). On the other hand, sample 15CIO09 (Haramul Mare dome) has a 25 % glomerocrysts content by volume, and 84 ± 35 % of its radiogenic argon originates from inherited argon (Table 4). A good correlation (Pearson correlation coefficient R ~ 0.95) exists between glomerocryst abundance and inherited radiogenic argon (Fig. 7). This correlation remains good even if the glomerocryst-free sample (of M. Puturosu) is omitted. The correlation between glomerocryst abundance and inherited radiogenic argon allows a corrected age for the Dealul Taţa dome to be derived. Thin section analysis of the same dome lava, as dated on whole rock at 430 ± 50 ka by Szakács et al. (2015), displays a 23 vol% glomerocryst content. It contains 85 ± 20 % of inherited argon (blue thin lines in Fig. 8) which implies an age of 64 ± 61 ka. This age is still poorly constrained but is consistent with those obtained here for the same area across which are younger than 144 ka (Fig. 1).

Some of our new K-Ar ages are in good agreement with published (U–Th)/He ages (Karátson et al. 2013; Harangi et al. 2015a; Molnár et al. 2018). For the M. Puturosu dome, the (U–Th)/He age of 642 ± 44 ka (Molnár et al. 2018) is similar to both the conventional K-Ar age of 710 ± 40 ka (Szakács et al. 2015) and our new K-Ar age of 704 ± 18 ka, which are all coeval at 2σ. Also, our new ages for the Balvanyos dome, 641 ± 9 ka and 440 ± 12 ka, are

similar to the 583 ± 30 ka (U-Th)/He age of Molnár et al. (2018). Note, however, that there is a strong alteration of the dome rocks of the Balvanyos summit, close to where the (U-Th)/He age was obtained (Molnár et al. 2018). Instead, both our dated samples were taken at the periphery of the dome from talus debris containing fresh rocks. Of these samples, the position of 16CIO07 is the most proximal to the dome, and therefore the 641 ± 9 ka date is that proposed to constrain the Balvanyos dome extrusion; overlapping with the 583 ± 30 ka (U-Th)/He age at 2σ.

The Haramul Mic dome was dated at 163 ± 11 ka by (U–Th)/He by Molnár et al. (2018). This is only slightly different (at 2σ) from our age obtained from plagioclase microphenocrysts (245 ± 24 ka). In this case, because our age was considered as a maximum, the younger (U–Th)/He age is more likely. The similar age obtained by both methods confirms the conclusion that the main lava dome activity of Ciomadul started at around 200 ka.

On the other hand, there are also a number of (U–Th)/He ages which are not in agreement with our dates. Of these, the results proposed for the Dealul Cetăţii dome are not coeval even at 2σ: 184 ± 5 ka (this study) and ca. 116 – 142 ka (Karátson et al., 2013). Also, the Piscul Pietros (Köves Ponk) dacitic dome yielded an age of 60 ± 5 ka (this study), which is older than the (U–Th)/He age obtained from zircon (42.9 + 1.4 - 1.5 ka) by Harangi et al. (2015b). In this latter case, that the (U–Th)/He age is possibly too young could be due to three reasons. First, the (U–Th)/He age is significantly lower than the 380 ka-long U–Th secular equilibrium (Farley et al. 2002), consequently it correction of the U-Th concentration at the scale of each dated zircon (Schmitt et al. 2010; Danisik et al. 2012), making the ages very sensitive to the accuracy of such a correction. Secondly, for the Piscul Pietros dome,

580 only four zircons were dated, and only the three oldest are coeval, thus the youngest age
581 should not be considered when calculating the average age. Using only the 3 coeval zircon
582 ages yields an age of about 46 ± 4 ka which is closer to, and compatible with, our K-Ar age at
583 2σ. Thirdly, extraneous argon from an incomplete removal of xenocrysts for the
584 overestimation of the K-Ar age, as well as partial loss of helium for the underestimation of
585 the (U–Th)/He age, cannot be totally excluded. However, extraneous Ar effects, based on
586 the careful sample preparation are considered minor, if not negligible.

587 6.3 Difference between groundmass and xenocryst mineral ages

588 To demonstrate the occurrence of inherited argon, a whole-rock age determination
589 was carried out for the Haramul Mare dome (sample 15CI009, Table 4) following our unspiked
590 K-Ar technique. Several K-bearing phases were also dated to identify which of them were the
591 most susceptible to bias by inherited argon (Table 5 and Fig. 8). With the exception of
592 plagioclase from M. Puturosu dome, all ages were significantly older than the groundmass
593 ages (Tables 2 and 5). Consequently, the younger the juvenile lava of the dome is, the more
594 important the influence of the xenocrysts is on the biased whole-rock age.

595 The effect of single-step or two-step separation has been assessed by processing two
596 aliquots of sample 15CIOO1. The groundmass obtained from single-step separation gave an
597 age of 202 ± 6 ka, whereas an age of 184 ± 5 ka (i.e. 10% younger) was obtained from the
598 two-step separation (Fig. 10). This age difference can be related to inherited argon from the
599 plagioclase fraction remaining after the single-step separation, assuming that the crystals
600 originate from grains larger than 0.125 mm, i.e. from the size range on the CSD plot that
601 corresponds to the mixing between grains from both grain-size populations (Fig. 4b). As the
602 plagioclases from the glomerocrysts are significantly older (~ 1.4 Ma, see below) than the

603 eruption age (184 ± 5 ka), even a tiny remnant of them within the dated groundmass will
604 produce an overestimated age.

605 The same issue of inherited glomerocrysts can also be encountered for the late-stage
606 pyroclastic deposits that drape the lower flanks of the Ciomadul dome complex (Karátson et
607 al., 2016). The BIX-2 block-and-ash flow deposit, ~3 km south of Lake St. Ana and ~1 km east
608 of Bixad village (Fig. 1), for instance, is considered younger than 50 ka (Vinkler et al., 2007;
609 Harangi et al., 2010; Karátson et al., 2016), whereas biotite phenocrysts contained within the
610 sample of lava-dome rock yielded an age of 561 ± 19 ka (15CIOX2), categorizing them as
611 xenocrysts. We note that this age is coeval with the age obtained from biotite xenocrysts
612 (569 ± 9 ka, Table 5) from the Dealul Cetăţii dome (184 ± 4 ka, Table 1 and Fig. 1) located 4
613 km to the north, suggesting that for both eruptions (BIX-2 block-and-ash flow and Dealul
614 Cetăţii dome) the xenocrysts were inherited material originating from the same crystal
615 mush.

616 The most extreme shift is encountered for the plagioclase glomerocrysts of the Vârful
617 Comlos dome (16CIO02, Table 5). These were dated at 1848 ± 27 ka, compared to 144 ± 4 ka
618 from the groundmass. Considering the freshness of the sample, the loss of potassium (which
619 would increase the age) can be ruled out and, consequently, these plagioclases are
620 considered as the oldest inherited phase incorporated in any rock sample of Ciomadul.
621 Notably, their old age is in the range obtained for the adjacent Pilişca volcano (Pécskay et al.,
622 1995; Szakács et al., 2015; Molnár et al., 2018; Karátson et al., this volume).

623 The presence of inherited glomerocrysts indicates that the dated lava dome samples
624 do not have a single crystallization age. Furthermore, theses lavas contain minerals having
625 experienced a multi-stage crystallization history, as also confirmed by the abundance of

626 oscillatory zoning in the larger plagioclase population (see, for instance, those in Fig. 3a).
627 Similar assimilation of inherited argon in plagioclase, hornblende and biotite has been
628 reported for the Youngest Toba Tuff eruption (74 ± 4 ka), where these minerals show K-Ar
629 ages predating the eruption by as much as 1.5 Ma (Gardner et al. 2002). In the context of
630 Ciomadul, it has previously been suggested that the crystal mush residing beneath the
631 volcano was rapidly (in < 100 y) remobilized by mafic magmas prior to the latest eruptions
632 after tens of thousands of years of quiescence (Harangi et al. 2015a), as also observed in
633 New Zealand at Taupo (Cole et al. 2014).

634 The following two arguments suggest that the older ages are due to the presence of
635 argon inherited from the most retentive mineral phases: (1) the rather good correlation
636 between K-Ar ages from the groundmass and the (U-Th)/He ages, and (2) the contrast
637 between groundmass ages and pure mineral phase ages. This latter contrast would not be so
638 important in case of a generalized contamination of the magma by excess argon. Indeed,
639 excess argon tends to be relatively uncommon in minerals from silicic volcanic rocks largely
640 because argon is highly incompatible in all major igneous minerals (Kelley 2002). As already
641 described for Ciomadul (Kiss et al. 2014) and elsewhere (Singer et al. 1998; Stewart 2010;
642 Doherty et al. 2012), the presence of glomerocrysts suggests a long-residence storage of
643 silicic crystal mush in an upper crustal storage zone about 8-12 km below the surface. This
644 may have been remobilized by any subsequent eruption of the dacitic magma (Kiss et al.
645 2014). At Ciomadul, our geochronological data show that a significant proportion of the
646 'phenocrysts' in the porphyritic dacites of Ciomadul are in fact old glomerocrysts.

647 Magma mixing is a widespread igneous phenomenon of variable importance,
648 particularly evident in systems where a vapor-saturated magma reservoir occurs (Anderson
649 1976). Such mixing between highly crystallized remnant magma of preceding activity with

650 newly injected hot magma prior to eruption has been observed in other volcanic settings
651 such as Unzen (Nakamura 1995), the Mascota - Amatlán de Cañas volcanic fields (Luhr et al.
652 1989; Gomez-Tuena et al. 2011) and the Palma Sola volcanic field (Gomez-Tuena et al. 2003)
653 in the Trans-Mexican Volcanic Belt volcanism. Of these cases, the Los Azufres volcanic field
654 (Mexico) shows evidence of the presence of a quartzo-feldspathic crystal-mush, located at a
655 depth of around 5 – 10 km (Rangel et al. 2018). Large sanidine, quartz, plagioclase, and
656 amphibole phenocrysts and mineral clots were assimilated from this mush by a melt
657 extraction process, probably triggered by the arrival of a hotter magma at the base of the
658 crystal-mush. This juvenile magma in turn caused reheating and partial melting of the
659 quartzo-feldspathic crystal-mush (Rangel et al. 2018).

660 The size effect of the analysed minerals has also been checked by dating of
661 plagioclases from samples 16CIO02, 16CIO04 and 16CIO09 (250-500 µm fraction from single-
662 step preparation and 63-125 µm fraction from two-step separation). In all cases (Table 5 and
663 Fig. 8), the larger-sized fraction size gave the oldest ages. This systematic shift toward older
664 ages of large grains substantiates that the population of large plagioclase crystals contains
665 inherited glomerocrysts. The case of sample 16CIO09 is extreme, as the small plagioclase
666 grains gave an age of 201 ± 5 ka, three times older than the groundmass age (60 ± 5 ka) but
667 also five times younger than that obtained on large plagioclase xenocrysts (981 ± 15 ka). This
668 finding implies that in the two-step fraction a significant amount of inherited plagioclase
669 remained in addition to juvenile minerals that crystallised during lava dome cooling. These
670 inherited minerals are either anhedral glomerocrysts (Fig. 3a), or euhedral and zoned
671 individual phenocrysts of plagioclase (Fig. 3a) that must have formed in the magma storage
672 system prior to eruption. Unfortunately, because of the contrast between eruption and
673 inherited mineral ages (which has a difference by a factor of up to 16 in sample 16CIO09),

674 even a small portion of inherited plagioclase remaining in the microphenocrystic fraction
675 extracted from the two-step separation will significantly increase the age obtained. This is
676 the reason why we suggest considering the ages obtained on plagioclase microphenocrysts
677 as maximum ages (16CIO01 on Haramul Mic and 16CIO04 on Ciomadul Mare domes). A
678 similar age range (1 Ma) between multiple dated fractions has been observed on a single
679 basaltic lava sample (from the Tihany Maar Volcanic Complex, Western Hungary) from eight
680 groundmass aliquots showing various density and magnetic properties (Balogh and Nemeth
681 2005). In this later case, due to a much older eruption age (7.92 ± 0.22 Ma), the difference
682 between the different dated fractions shows less contrast (only 20% of excess). However, as
683 in our study, the oldest age comes from aliquots showing the highest contamination by
684 inherited minerals, while the groundmass aliquot, whose age is closest to that of the
685 eruption, i.e. almost free of inherited minerals, is light and magnetic.

686 6.4 Magmatic origin of inherited minerals

687 The apparent presence of inherited argon in the minerals of Ciomadul leads to
688 questions regarding their origin with respect to the argon diffusion law in silicate minerals.
689 Closure temperatures calculated for volume diffusion (e.g. Dodson, 1973) predict that at
690 supra-solidus temperatures, and with extended residence time (> 1 ky), every major mineral
691 phase in these magmas should have remained fully open to argon loss prior to eruption. To
692 explain the presence of inherited argon in magmas, it has been suggested that the
693 incompletely reset minerals were xenocrysts with short (~ 10 years) residence times
694 (Gansecki et al., 1996; Singer et al., 1998; Gardner et al., 2002). This mechanism is
695 particularly likely for relatively small (< 10 km^3) magma bodies (Singer et al. 1998), such as
696 those of Ciomadul. Similar processes operating over similar time scales has been observed at

697 different volcanic context, for instance : (1) the Taupo Volcanic Zone, New Zealand, where a
698 large variations in crystallinity and long magma time residence (up to 250 ky, i.e. same order
699 of magnitude as in Ciomadul) are shown (e.g. Brown et al., 1998; Brown and Fletcher, 1999;
700 Matthews et al., 2012); (2) ongoing eruption of Unzen (Japan) where dacite is formed by
701 mixing of relatively high- and low-temperature end-member magmas (Nakamura 1995;
702 Nishimura et al. 2005). Thermo-mechanical considerations suggest that an effective
703 reactivation of crystal mush is possible when the melt content in the magma reservoir
704 increases to ~60%, allowing eruptible magma to coalesce (Bachmann and Bergantz 2004;
705 Huber et al. 2011).

706 At Ciomadul, the source of glomerocrysts may be from previous crystallised magma of
707 Ciomadul, i.e. from a disrupted crystal mush (Kiss et al., 2014). The thermobarometrical
708 analysis of amphibole (hornblende and pargasite) crystallisation present in Ciomadul rocks
709 shows that hornblende is xenocrystic, despite the importance of this phase in some domes
710 (Kiss et al. 2014). Plagioclase is present both as inherited glomerocrysts and phenocrysts,
711 because it displays ages either older than (samples 15CIO01, 16CIO02, 16CIO09) or similar
712 (16CIO08) to the groundmass ages. Crystal clots of hornblende and plagioclase observed in
713 some domes (samples 15CIO01, 16CIO02, 16CIO03, 16CIO04, and 16CIO09) suggest that the
714 glomerocrystic material came from sources up to 1.85 Ma old (the oldest age obtained at
715 Ciomadul). Such populations of older crystals contain variably argon-inherited content,
716 explaining spuriously old ages that are common in differentiated lava domes in an arc
717 context (Harford et al. 2002; Zimmerer et al. 2016).

718 The dominant mechanism for the generation of kinked CSD profiles is magma mixing.
719 This preserves a steep slope for small-sized grains and adds a gentler slope for larger sized
720 crystals, regardless of their proportions (Higgins, 2006). The larger population

(phenocrysts/glomerocrysts) can be identified as crystals inherited from one of the parental magmas (crystal mush), whereas the finer population (microphenocrysts) originated from the juvenile parent magma, in addition to the microlitic groundmass. Profiles of CSD data that are particularly kinked validate such a scenario. The fact that both mafic mineral phases and plagioclase show exceedingly similar kinked CSD spectra (i.e. an abnormally large amount of coarse grains) in the Ciomadul lavas strongly supports deep-seated storage as a common feature of this magmatic contribution (Armienti et al. 1994).

The oldest reliable eruption age of the dacitic domes of Ciomadul is around 700 ka (Muntele Puturosu dacitic dome). Another Ciomadul-type dacite dome adjacent to the Pilişca volcano, Bába Laposa (942 ± 65 ka), and the andesitic dome of Dealul Mare (842±53 ka), both dated by (U-Th)/He method (Molnár et al., 2018), are just slightly older. Therefore, the old age obtained on the inherited plagioclase phase (1.85 Ma) points to assimilation of xenocrysts from earlier magmatism, possibly that of the Pilişca volcano itself (Fig. 1). Incorporation of quite old xenocrysts from a crystal mush into dacitic magmas similar to those of Ciomadul has been observed in other volcanic systems. For instance, Nevado de Toluca (Mexico) experienced an eruption at ~13 ka where biotite, up to 4 Ma old, was incorporated and resided in the magma for only a short period of time before it erupted (Arce et al. 2006). One can note that in this example, as well as at Ciomadul, mafic-intermediate magma replenished the system since ~ 1 Ma and contributed to the eruption of new domes as well as effusive-explosive activity (Torres-Orozco et al., 2017a).

From amphibole thermobarometrical studies, Kiss et al. (2014) suggested a complex and multi-zonal context of polybaric crystallization of amphibole in the mid- to upper crust beneath Ciomadul. Crystallisation of these minerals occurred in a long-lived shallow storage zone (possibly shared with the neighbouring Pilişca volcano) filled with a cold crystal mush

745 (Kiss et al. 2014) that was subsequently remobilized by the injection of a hot mafic magma,
746 as observed at Unzen, Montserrat or Ruapehu volcanoes (Nakamura 1995; Murphy et al.
747 2000; Gamble et al. 2003).

748 Repose periods as long as those occurring between Ciodamul eruptions are frequently
749 observed at these volcanoes fed by intermediate magmas. Illustrated by zircon
750 crystallization ages ranging from 10s to 100s of thousands of years, these volcanoes have
751 experienced prolonged and recurrent presence of melt-bearing magma (Cooper and Reid
752 2008; Schmitt et al. 2010; Reid et al. 2011; Rubin et al. 2016). The operation of such volcanic
753 plumbing systems generates a large amount of glomerocrystic aggregates made up of
754 minerals, which begin to store radiogenic argon prior to eruption. At Ciomadul, at the depth
755 of 8-12 km proposed by Kiss et al. (2014), the expected crystal-mush temperatures (240 –
756 300 °C) are in the same order of magnitude as the closure temperature for argon gas in the
757 mineral constituting the crystal clots: ~ 225-300 °C for plagioclase, ~ 350 °C for biotite and K-
758 feldspar, and ~ 600 °C for hornblende (assuming a cooling rate of 10°C/Ma; e.g. McDougall
759 and Harrison, 1999; Cassata et al., 2009; Baxter, 2010). Consequently, these minerals likely
760 began to store radiogenic argon in the crystal mush prior to the eruption. The newly injected
761 magma batches of Ciomadul's eruptions, provided the heat to remobilise the crystal mush
762 and its constituent mineral phases that had crystallised earlier from an evolved (silica-rich)
763 magma. The biotite ages are significantly younger than those obtained on plagioclase and
764 amphibole (Fig. 9). This can be interpreted as reflecting either a difference in the crystal clot
765 ages from which the mineral originated (younger for biotite than plagioclase/amphibole).
766 Alternatively, it may reflect a different behaviour of these minerals which come from a single
767 source but which have a contrasting response to argon degassing when they are in contact
768 with the replenishing magma. The former hypothesis is more speculative as incorporation of

769 xenocrysts would include all mineral phases present in the crystal mush without segregation,
770 whereas the latter is easily obtained by consideration of diffusion processes.

771 The coexistence of hornblende and plagioclase in the crystal clots support the
772 interpretation that the xenocrysts came from the same-aged source, and the diffusional Ar
773 loss model implies a complete reset of radiogenic argon in the plagioclases (Gardner et al.,
774 2002). Such results from the 74 ka Toba Tuff were interpreted incompatible with a long
775 storage of xenocrystic minerals in the magma reservoir but, instead, were explained by
776 contamination of the plutonic crystals, preceding the eruption by only a few years (Gardner
777 et al. 2002). Models of diffusion in similar contexts (Gansecki et al. 1996; Gardner et al.
778 2002; Bachmann et al. 2007) suggest that the magma of most Ciomadul monogenetic domes
779 assimilated the solidified and cooled crystal-mush material (with trapped argon) shortly
780 before extrusion. Consequently, the more than doubling of the xenocryst volume in the
781 Ciomadul lava domes with time (from an average of 7% at 700 ka to ~ 17% at 60 ka, Fig. 11)
782 can be interpreted as increasing assimilation of crystal mush, as it became increasingly
783 fragmented and remobilised (Fig. 11).

784 6.5 Geochemical evolution of the Ciomadul lava domes

785 With regard to the new geochronological constraints, we can consider the main
786 petrological and geochemical features of magma evolution through time. Samples with ages
787 > 450 ka seem to be characterized by a higher concentration (~23 vol.%) of plagioclase
788 crystals, whereas their concentration slightly decreases toward the younger domes (~ 15 %)
789 (Fig. 11). This can be attributed to shorter magmatic storage for the progressively younger
790 rocks, limiting the growth of large plagioclase phenocrysts. On the other hand, over the 700

791 ky long history of Ciomadul's effusive volcanism, the proportion of xenocrysts or
792 glomerocrystic aggregates slightly increases with time (Fig. 11).

793 While small groundmass microlites grew from their carrier liquid during the final phase
794 of pre-eruptive or post-eruptive crystallization, large glomerocrysts were entrained from a
795 crystal mush. Material erupted in later episodes contains proportionally more mush-derived
796 material (Fig. 11), in relation to a larger amount of assimilation of the silicic crystal mush
797 located beneath the volcano (cf. Kiss et al., 2014). Changes in phase proportions (Table 4 and
798 Fig. 11) between Ciomadul eruptions highlight an increase of the glomerocryst entrainment
799 efficiency during the whole Ciomadul history. With time, the proportion of crystal mush,
800 fragmented during interaction with the new magma, increases. This induces an increasing
801 mobility of the glomerocrysts, allowing them to be more readily remobilised, and eventually
802 assimilated, during the injection of fresh magma. Such a scenario would explain the
803 inherited argon increase through time as more and more inherited crystals are incorporated
804 into the magma reaching the surface (Fig. 11).

805 Since 250 ka (i.e. over the main phase of Ciomadul dome activity), a temporal
806 evolution in major element oxide concentrations can be seen (Fig. 12). With time, SiO_2 and
807 Na_2O concentrations significantly increase, as does, to a lesser extent, K_2O. On the other
808 hand, elements such as Fe_2O_3, MgO, as well as Al_2O_3, CaO and TiO_2 concentrations slightly
809 decrease. The evolution through time for these oxides highlights the effect of fractional
810 crystallization and the increase of the influence of crystal mush assimilation since 250 ka.
811 The relatively good correlation between the degree of differentiation and time, as well as
812 the general trends in the major element data, support a dual control by crystal-melt
813 fractionation and crystal mush assimilation. Slightly decreasing of the plagioclase content
814 through time as well as the concentrations of CaO and Al_2O_3 could be considered as

paradoxical. However, geochemical data provided here are from whole-rock, i.e. from crystal-rich lavas where both plagioclase phenocrysts and xenocrysts influence element oxide concentration. Consequently, the total concentration of plagioclase (phenocryst + xenocryst) present in the lavas increases through time, which is in accordance with the expected behaviour of CaO and Al_2O_3.

7 Conclusions

New unspiked K-Ar dates acquired mostly from the groundmass of lava samples, complemented by major elements geochemistry, provide new insights into the geochronological evolution of the extrusive history of the Late Quaternary Ciomadul volcano. Our dating effort mainly focused on the central, most voluminous, part of Ciomadul, which was hitherto poorly constrained. Following a rigorous process of sample selection and preparation by a two-step separation, we managed to obtain groundmass aliquots avoiding any traces of xenocrysts. Most ages obtained on these groundmass fractions contradict those obtained by whole-rock K-Ar dating reported in previous studies and largely agree with (U-Th)-He ages. Based on the new results, the timing of the extrusive activity at Ciomadul can be summarised as follows: 1) a first stage from ca. 850 ka to 440 ka during which minor extrusive activity occurred in the area of the Puturosu Hills; followed by 2) a shorter but more voluminous second stage from ca. 200 ka to 30 ka. During this second stage, volcanism began (between ca. 200 ka to 130 ka) when the northern and western-central parts of Ciomadul were constructed. Then, after a few tens of thousands of years of quiescence, predominantly effusive activity resumed at ~ 100 ka when the eastern-central part of the dome complex grew. This second phase of activity partly overlapped with the final, highly explosive eruptive phase that began at ~ 51 ka and ended around 29 ka

838 (Karátson et al. 2016). As the current quiescence period of the volcano is shorter than
839 quiescence periods occurring in its earlier history, Ciomadul cannot be considered extinct.

840 In addition to the groundmass ages presented here, dating efforts focussing on pure
841 mineral phases highlight that a large amount of inherited argon is responsible for the
842 obvious shift from the systematically older whole-rock to the younger groundmass ages,
843 showing a more or less linear relationship between excess argon and the abundance of
844 inherited crystals. These crystals are more abundant in the younger rocks, indicating
845 increasing contamination of magma by inherited crystals from a crystal mush during volcanic
846 activity at Ciomadul. Some of the inherited crystals must have formed up to 2 Ma ago and
847 may be associated with the neighbouring Pilişca volcano. Such a dual source of composition
848 for the erupted material is noticeable on the kinked CSD plots of the Ciomadul dacitic lavas.
849 Contrasting behaviour of the mineral phases during partial degassing inside the crystal mush,
850 from their formation to the eruption and during their incorporation into the juvenile magma,
851 can explain the wide range of ages obtained in a single sample. Comparison with the
852 geochemical data suggests a magmatic evolution towards more SiO_2-rich products and
853 increasing assimilation and incorporation with time of an earlier-formed crystal mush.

854 In summary, Ciomadul's initial, sporadic dome extrusions in the SE of the volcanic
855 complex were followed by much larger scale extrusive activity in the central part. The good
856 spatial resolution of the obtained ages provides the basis for an assessment of magma
857 extrusion volumes through time (Karátson et al., this volume). The rigorous sample
858 preparation methodology, the small errors, and a complete analysis of all previously
859 published radiometric ages, validates the reliability of the newly obtained K-Ar ages. This
860 approach, when coupled with CSD and geochemical studies, demonstrates how such an

integrated approach can inform on the evolution of magmatic systems, the activity they feed, and the time scales of evolution over hundreds to hundreds-of-thousands of years

Acknowledgements

We wish to thank Karoly Nemeth and an anonymous reviewer, as well as Editors Stephen Self and Andrew Harris for their comments and suggestions, which greatly helped us to improve the clarity of the manuscript. This research was supported by the Hungarian Scientific Research Fund NKFIH - OTKA No. K 115472 to DK. Fruitful discussions with Carlos Palares and Xavier Quidelleur at different stages of this study have helped to clarify the ideas presented in this paper. This is Laboratoire de Géochronologie Multi-Techniques (LGMT) contribution number 146.

References

Anderson A (1976) Magma mixing - petrological process and volcanological tool. J Volcanol Geotherm Res 1:3–33. doi: 10.1016/0377-0273(76)90016-0

Arce JL, Macias JL, Gardner JE, Layer PW (2006) A 2.5 ka history of dacitic magmatism at Nevado de Toluca, Mexico: Petrological, Ar-40/Ar-39 dating, and experimental constraints on petrogenesis. J Petrol 47:457–479. doi: 10.1093/petrology/egi082

Armienti P, Pareschi M, Innocenti F, Pompilio M (1994) Effects of magma storage and ascent on the kinetics of crystal-growth - the case of the 1991-93 Mt Etna eruption. Contrib Mineral Petrol 115:402–414. doi: 10.1007/BF00320974

Bachmann O, Bergantz GW (2004) On the origin of crystal-poor rhyolites: Extracted from batholithic crystal mushes. J Petrol 45:1565–1582. doi: 10.1093/petrology/egh019

Bachmann O, Oberli F, Dungan MA, et al (2007) (40)Ar/(39)Ar and U-Pb dating of the Fish Canyon magmatic system, San Juan Volcanic field, Colorado: Evidence for an extended crystallization history. Chem Geol 236:134–166. doi: 10.1016/j.chemgeo.2006.09.005

Balogh K, Nemeth K (2005) Evidence for the neogene small-volume intracontinental. volcanism in western hungary: K/Ar geochronology of the Tihany Maar volcanic complex. Geol Carpathica 56:91–99

889 Balogh K, Nemeth K, Itaya T, et al (2010) Loss of Ar-40(rad) from leucite-bearing basanite at
890 low temperature: implications on K/Ar dating. Cent Eur J Geosci 2:385–398. doi:
891 10.2478/v10085-010-0026-3

892 Baxter EF (2010) Diffusion of Noble Gases in Minerals. In: Zhang YX, Cherniak DJ (eds)
893 Diffusion in Minerals and Melts. pp 509–557

894 Blake S (1990) Viscoplastic models of lava domes

895 Boven A, Pasteels P, Kelley SP, et al (2001) Ar-40/Ar-39 study of plagioclases from the
896 Rogaland anorthosite complex (SW Norway); an attempt to understand argon ages in
897 plutonic plagioclase. Chem Geol 176:105–135. doi: 10.1016/S0009-2541(00)00372-7

898 Brown SJA, Fletcher IR (1999) SHRIMP U-Pb dating of the preeruption growth history of
899 zircons from the 340 ka Whakamaru Ignimbrite, New Zealand: Evidence for > 250 k.y.
900 magma residence times. Geology 27:1035–1038. doi: 10.1130/0091-
901 7613(1999)027<1035:SUPDOT>2.3.CO;2

902 Brown SJA, Wilson CJN, Cole JW, Wooden J (1998) The Whakamaru group ignimbrites, Taupo
903 Volcanic Zone, New Zealand: evidence for reverse tapping of a zoned silicic magmatic
904 system. J Volcanol Geotherm Res 84:1–37. doi: 10.1016/S0377-0273(98)00020-1

905 Cadoux A, Pinti DL, Aznar C, et al (2005) New chronological and geochemical constraints on
906 the genesis and geological evolution of Ponza and Palmarola Volcanic Islands
907 (Tyrrhenian Sea, Italy). LITHOS 81:121. doi: 10.1016/j.lithos.2004.09.020

908 Calvert AT, Moore RB, McGeehin JP, Rodrigues da Silva AM (2006) Volcanic history and Ar-
909 40/Ar-39 and C-14 geochronology of Terceira Island, Azores, Portugal. J Volcanol
910 Geotherm Res 156:103–115. doi: 10.1016/j.jvolgeores.2006.03.016

911 Cassata WS, Renne PR, Shuster DL (2009) Argon diffusion in plagioclase and implications for
912 thermochronometry: A case study from the Bushveld Complex, South Africa.
913 Geochim Cosmochim Acta 73:6600–6612. doi: 10.1016/j.gca.2009.07.017

914 Cassignol C, Gillot P-Y (1982) Range and effectiveness of unspiked potassium-argon dating:
915 experimental groundwork and applications. In: Numerical Dating in Stratigraphy,
916 John Wiley & Sons. Odin G.S., pp 159–179

917 Cole JW, Deering CD, Burt RM, et al (2014) Okataina Volcanic Centre, Taupo Volcanic Zone,
918 New Zealand: A review of volcanism and synchronous pluton development in an
919 active, dominantly silicic caldera system. Earth-Sci Rev 128:1–17. doi:
920 10.1016/j.earscirev.2013.10.008

921 Condit CD, Connor CB (1996) Recurrence rates of volcanism in basaltic volcanic fields: An
922 example from the Springerville volcanic field, Arizona. Geol Soc Am Bull 108:1225–
923 1241. doi: 10.1130/0016-7606(1996)108<1225:RROVIB>2.3.CO;2

924 Connor CB, Hill BE (1995) 3 nonhomogeneous Poisson models for the probability of basaltic
925 volcanism - application to the Yucca Mountain region, Nevada. J Geophys Res-Solid
926 Earth 100:10107–10125. doi: 10.1029/95JB01055

927 Cooper KM, Reid MR (2008) Uranium-series Crystal Ages. In: Putirka KD, Tepley FJ (eds)
928 Minerals, Inclusions and Volcanic Processes. pp 479–544

929 Coulie E, Quidelleur X, Gillot PY, et al (2003) Comparative K-Ar and Ar/Ar dating of Ethiopian
930 and Yemenite Oligocene volcanism: implications for timing and duration of the
931 Ethiopian traps. Earth Planet Sci Lett 206:477–492. doi: 10.1016/S0012-
932 821X(02)01089-0

933 Crisp J (1984) Rates of magma emplacement and volcanic output. J Volcanol Geotherm Res
934 20:177–211. doi: 10.1016/0377-0273(84)90039-8

935 Dalrymple G, Moore J (1968) Argon-40 - excess in submarine pillow basalts from Kilauea
936 volcano Hawaii. Science 161:1132-+. doi: 10.1126/science.161.3846.1132

937 Damaschke M, Cronin SJ, Bebbington MS (2018) A volcanic event forecasting model for
938 multiple tephra records, demonstrated on Mt. Taranaki, New Zealand. Bull Volcanol
939 80:9. doi: 10.1007/s00445-017-1184-y

940 Danisik M, Shane P, Schmitt AK, et al (2012) Re-anchoring the late Pleistocene
941 tephrochronology of New Zealand based on concordant radiocarbon ages and
942 combined U-238/Th-230 disequilibrium and (U-Th)/He zircon ages. Earth Planet Sci
943 Lett 349:240–250. doi: 10.1016/j.epsl.2012.06.041

944 Dodson MH (1973) Closure temperature in cooling geochronological and petrological
945 systems. Contrib Mineral Petrol 40:259–274. doi: 10.1007/BF00373790

946 Doherty AL, Bodnar RJ, De Vivo B, et al (2012) Bulk rock composition and geochemistry of
947 olivine-hosted melt inclusions in the Grey Porri Tuff and selected lavas of the Monte
948 dei Porri volcano, Salina, Aeolian Islands, southern Italy. Cent Eur J Geosci 4:338–355.
949 doi: 10.2478/s13533-011-0066-7

950 Farley KA, Kohn BP, Pillans B (2002) The effects of secular disequilibrium on (U-Th)/He
951 systematics and dating of Quaternary volcanic zircon and apatite. Earth Planet Sci
952 Lett 201:117–125. doi: 10.1016/S0012-821X(02)00659-3

953 Gamble JA, Price RC, Smith IEM, et al (2003) Ar-40/Ar-39 geochronology of magmatic
954 activity, magma flux and hazards at Ruapehu volcano, Taupo Volcanic Zone, New
955 Zealand. J Volcanol Geotherm Res 120:271–287. doi: 10.1016/S0377-0273(02)00407-
956 9

957 Gansecki CA, Mahood GA, McWilliams MO (1996) Ar-40/Ar-39 geochronology of rhyolites
958 erupted following collapse of the Yellowstone caldera, Yellowstone Plateau volcanic
959 field: Implications for crustal contamination. Earth Planet Sci Lett 142:91–107. doi:
960 10.1016/0012-821X(96)00088-X

961 Gardner JE, Layer PW, Rutherford MJ (2002) Phenocrysts versus xenocrysts in the youngest
962 Toba Tuff: Implications for the petrogenesis of 2800 km(3) of magma. Geology
963 30:347–350. doi: 10.1130/0091-7613(2002)030<0347:PVXITY>2.0.CO;2

964 Germa A, Lahitte P, Quidelleur X (2015) Construction and destruction of Mont Pelee volcano:
965 Volumes and rates constrained from a geomorphological model of evolution. J
966 Geophys Res-Earth Surf 120:1206–1226. doi: 10.1002/2014JF003355

967 Germa A, Quidelleur X, Labanieh S, et al (2010) The eruptive history of Morne Jacob volcano
968 (Martinique Island, French West Indies): Geochronology, geomorphology and
969 geochemistry of the earliest volcanism in the recent Lesser Antilles arc. J Volcanol
970 Geotherm Res 198:297–310. doi: 10.1016/j.jvolgeores.2010.09.013

971 Germa A, Quidelleur X, Labanieh S, et al (2011a) The volcanic evolution of Martinique Island:
972 Insights from K-Ar dating into the Lesser Antilles arc migration since the Oligocene. J
973 Volcanol Geotherm Res 208:122–135. doi: 10.1016/j.jvolgeores.2011.09.007

974 Germa A, Quidelleur X, Lahitte P, et al (2011b) The K-Ar Cassignol-Gillot technique applied to
975 western Martinique lavas: A record of Lesser Antilles arc activity from 2 Ma to Mount
976 Pelee volcanism. Quat Geochronol 6:341–355. doi: 10.1016/j.quageo.2011.02.001

977 Gertisser R, Charbonnier SJ, Keller J, Quidelleur X (2012) The geological evolution of Merapi
978 volcano, Central Java, Indonesia. Bull Volcanol 74:1213–1233. doi: 10.1007/s00445-
979 012-0591-3

980 Gillot P-Y, Cornette Y (1986) The Cassignol technique for potassium - argon dating, precision
981 and accuracy - examples from the late Pleistocene to recent volcanics from southern
982 Italy. Chem Geol 59:205–222

983 Gillot P-Y, Cornette Y, Max N, Floris B (1992) Two reference materials, trachytes MDO-G and
984 ISH-G, for argon dating (KeAr and 40Ar/39Ar) of Pleistocene and Holocene rocks.
985 Geostand Newsl 16:55–60. doi: 10.1111/j.1751-908X.1992.tb00487.x

986 Gillot P-Y, Hildenbrand A, Lefevre JC, Albore-Livadie C (2006) The K/Ar dating method:
987 principle, analytical techniques, and application to Holocene volcanic eruptions in
988 southern Italy. Acta Vulcanol 18:55–66

989 Gomez-Tuena A, LaGatta AB, Langmuir CH, et al (2003) Temporal control of subduction
990 magmatism in the eastern Trans-Mexican Volcanic Belt: Mantle sources, slab
991 contributions, and crustal contamination. Geochem Geophys Geosystems 4:8912.
992 doi: 10.1029/2003GC000524

993 Gomez-Tuena A, Mori L, Goldstein SL, Perez-Arvizu O (2011) Magmatic diversity of western
994 Mexico as a function of metamorphic transformations in the subducted oceanic
995 plate. Geochim Cosmochim Acta 75:213–241. doi: 10.1016/j.gca.2010.09.029

996 Harangi S, Lenkey L (2007) Genesis of the Neogene to Quaternary volcanism in the
997 Carpathian-Pannonian region: Role of subduction, extension, and mantle plume. In:

998 Beccaluva L, Bianchini G, Wilson M (eds) Cenozoic Volcanism in the Mediterranean
999 Area. pp 67–92

1000 Harangi S, Lukács R, Schmitt AK, et al (2015a) Constraints on the timing of Quaternary
1001 volcanism and duration of magma residence at Ciomadul volcano, east–central
1002 Europe, from combined U–Th/He and U–Th zircon geochronology. J Volcanol
1003 Geotherm Res 301:66–80. doi: 10.1016/j.jvolgeores.2015.05.002

1004 Harangi S, Molnár M, Vinkler AP, et al (2010) Radiocarbon dating of the last volcanic
1005 eruptions of Ciomadul volcano, Southeast Carpathians, eastern-central Europe.
1006 Radiocarbon 52:1498–1507

1007 Harangi S, Novák A, Kiss B, et al (2015b) Combined magnetotelluric and petrologic constrains
1008 for the nature of the magma storage system beneath the Late Pleistocene Ciomadul
1009 volcano (SE Carpathians). J Volcanol Geotherm Res 290:82–96. doi:
1010 10.1016/j.jvolgeores.2014.12.006

1011 Harford C, Pringle MS, Sparks RSJ, Young SR (2002) The volcanic evolution of Montserrat
1012 using 40Ar/39Ar geochronology. In: The Eruption of Soufrière Hills Volcano,
1013 Montserrat, from 1995 to 1999, The Geological Society Memoirs. Druitt, T.H.,
1014 Kokelaar, B.P., London, pp 93–113

1015 Heizler MT, Perry FV, Crowe BM, et al (1999) The age of Lathrop Wells volcanic center: An
1016 Ar-40/Ar-39 dating investigation. J Geophys Res-Solid Earth 104:767–804. doi:
1017 10.1029/1998JB900002

1018 Higgins MD (1996) Crystal size distributions and other quantitative textural measurements in
1019 lavas and tuff from Egmont volcano (Mt Taranaki), New Zealand. Bull Volcanol
1020 58:194–204. doi: 10.1007/s004450050135

1021 Higgins MD (2002) Closure in crystal size distributions (CSD), verification of CSD calculations,
1022 and the significance of CSD fans. Am Mineral 87:171–175

1023 Higgins MD (2006) Quantitative Textural Measurements in Igneous and Metamorphic
1024 Petrology

1025 Higgins MD, Roberge J (2007) Three magmatic components in the 1973 eruption of Eldfell
1026 volcano, Iceland: Evidence from plagioclase crystal size distribution (CSD) and
1027 geochemistry. J Volcanol Geotherm Res 161:247–260. doi:
1028 10.1016/j.jvolgeores.2006.12.002

1029 Hildenbrand A, Weis D, Madureira P, Marques FO (2014) Recent plate re-organization at the
1030 Azores Triple Junction: Evidence from combined geochemical and geochronological
1031 data on Faial, S.Jorge and Terceira volcanic islands. Lithos 210:27–39. doi:
1032 10.1016/j.lithos2014.09.009

1033 Hildenbrand I Anthony; Gillot, Pierre-Yves; Le Roy (2004) Volcano-tectonic and geochemical
1034 evolution of an oceanic intra-plate volcano: Tahiti-Nui (French Polynesia)

1035 Hofmann C, Feraud G, Courtillot V (2000) Ar-40/Ar-39 dating of mineral separates and whole
1036 rocks from the Western Ghats lava pile: further constraints on duration and age of
1037 the Deccan traps. Earth Planet Sci Lett 180:13–27. doi: 10.1016/S0012-
1038 821X(00)00159-X

1039 Hora JM, Singer BS, Woerner G (2007) Volcano evolution and eruptive flux on the thick crust
1040 of the Andean Central Volcanic Zone: Ar-40/Ar-39 constraints from Volcan
1041 Parinacota, Chile. Geol Soc Am Bull 119:343–362. doi: 10.1130/B25954.1

1042 Huber C, Bachmann O, Dufek J (2011) Thermo-mechanical reactivation of locked crystal
1043 mushes: Melting-induced internal fracturing and assimilation processes in magmas.
1044 Earth Planet Sci Lett 304:443–454. doi: 10.1016/j.epsl.2011.02.022

1045 Karátson D, Telbisz T, Harangi S, et al (2013) Morphometrical and geochronological
1046 constraints on the youngest eruptive activity in East-Central Europe at the Ciomadul
1047 (Csomad) lava dome complex, East Carpathians. J Volcanol Geotherm Res 255:43–56.
1048 doi: 10.1016/j.jvolgeores.2013.01.013

1049 Karátson D, Timár G (2005) Comparative volumetric calculations of two segments of the
1050 Carpathian Neogene/Quaternary volcanic chain using SRTM elevation data:
1051 implications for erosion and magma output rates. In: Thouret JC, Chester DK (eds)
1052 Volcanic Landforms, Processes and Hazards. pp 19–35

1053 Karátson D, Wulf S, Veres D, et al (2016) The latest explosive eruptions of Ciomadul
1054 (Csomad) volcano, East Carpathians - A tephrostratigraphic approach for the 51-29 ka
1055 BP time interval. J Volcanol Geotherm Res 319:29–51. doi:
1056 10.1016/j.jvolgeores.2016.03.005

1057 Kelley S (2002) Excess argon in K-Ar and Ar-Ar geochronology. Chem Geol 188:1–22. doi:
1058 10.1016/S0009-2541(02)00064-5

1059 Kereszturi G, Bebbington M, Nemeth K (2017) Forecasting transitions in monogenetic
1060 eruptions using the geologic record. Geology 45:283–286. doi: 10.1130/G38596.1

1061 Kersting AB, Arculus PJ (1994) Klyuchevskoy volcano, Kamchatka, Russia - the role of high-
1062 flux recharged, tapped, and fractionated magma chamber(s) in the genesis of high-
1063 AL2O3 from high-MgO basalt. J Petrol 35:1–41

1064 Kis B-M, Ionescu A, Cardellini C, et al (2017) Quantification of carbon dioxide emissions of
1065 Ciomadul, the youngest volcano of the Carpathian-Pannonian Region (Eastern-
1066 Central Europe, Romania). J Volcanol Geotherm Res 341:119–130. doi:
1067 10.1016/j.jvolgeores.2017.05.025

1068 Kiss B, Harangi S, Ntaflos T, et al (2014) Amphibole perspective to unravel pre-eruptive
1069 processes and conditions in volcanic plumbing systems beneath intermediate arc
1070 volcanoes: a case study from Ciomadul volcano (SE Carpathians). Contrib Mineral
1071 Petrol 167:. doi: 10.1007/s00410-014-0986-6

1072 Lahitte P, Coulie E, Mercier N, et al (2001) K-Ar and TL volcanism chronology of the southern
1073 ends of the Red Sea spreading in Afar since 300 ka. Comptes Rendus Acad Sci Ser Ii
1074 Fasc -Sci 332:13–20. doi: 10.1016/S1251-8050(00)01491-9

1075 Lahitte P, Samper A, Quidelleur X (2012) DEM-based reconstruction of southern Basse-Terre
1076 volcanoes (Guadeloupe archipelago, FWI): Contribution to the Lesser Antilles Arc
1077 construction rates and magma production. Geomorphology 136:148–164. doi:
1078 10.1016/j.geomorph.2011.04.008

1079 Lexa J, Seghedi I, Nemeth K, et al (2010) Neogene-Quaternary Volcanic forms in the
1080 Carpathian-Pannonian Region: a review. Cent Eur J Geosci 2:207-U75. doi:
1081 10.2478/v10085-010-0024-5

1082 Luhr JF, Allan J, Carmichael I, et al (1989) Primitive calc-alkaline and alkaline rock types from
1083 the Western Mexican Volcanic Belt. J Geophys Res-Solid Earth Planets 94:4515–4530.
1084 doi: 10.1029/JB094iB04p04515

1085 Marsh BD (1988) Crystal size distribution (CSD) in rocks and the kinetics and dynamics.
1086 Contrib Mineral Petrol 99:277–291. doi: 10.1007/BF00375362

1087 Marzocchi W, Zaccarelli L (2006) A quantitative model for the time-size distribution of
1088 eruptions. J Geophys Res-Solid Earth 111:B04204. doi: 10.1029/2005JB003709

1089 Matenco L, Bertotti G, Leever K, et al (2007) Large-scale deformation in a locked collisional
1090 boundary: Interplay between subsidence and uplift, intraplate stress, and inherited
1091 lithospheric structure in the late stage of the SE Carpathians evolution. Tectonics
1092 26:TC4011. doi: 10.1029/2006TC001951

1093 Matthews NE, Pyle DM, Smith VC, et al (2012) Quartz zoning and the pre-eruptive evolution
1094 of the similar to 340-ka Whakamaru magma systems, New Zealand. Contrib Mineral
1095 Petrol 163:87–107. doi: 10.1007/s00410-011-0660-1

1096 McDougall I, Harrison TM (1999) Geochronology and Thermochronology by the 40Ar/39Ar
1097 Method, 2nd edn; Oxford University Press, New York

1098 Mock A, Jerram DA (2005) Crystal size distributions (CSD) in three dimensions: Insights from
1099 the. J Petrol 46:1525–1541. doi: 10.1093/petrology/egi024

1100 Molnár K, Harangi S, Lukács R, et al (2018) The onset of the volcanism in the Ciomadul
1101 Volcanic Dome Complex (Eastern Carpathians): Eruption chronology and magma type
1102 variation. J Volcanol Geotherm Res. doi:
1103 https://doi.org/10.1016/j.jvolgeores.2018.01.025

1104 Morgan DJ, Jerram DA (2006) On estimating crystal shape for crystal size distribution
1105 analysis. J Volcanol Geotherm Res 154:1–7. doi: 10.1016/j.jvolgeores.2005.09.016

1106 Moriya I, Okuno M, Nakamura T, et al (1996) Radiocarbon ages of charcoal fragments from
1107 the pumice flow deposit of the last eruption of Ciomadul volcano, Romania. In:
1108 Summaries of Researches using AMS. Nagoya University 7, pp 255–257

1109 Murphy MD, Sparks RSJ, Barclay J, et al (2000) Remobilization of andesite magma by
1110 intrusion of mafic magma at the Soufriere Hills Volcano, Montserrat, West Indies. J
1111 Petrol 41:21–42. doi: 10.1093/petrology/41.1.21

1112 Nakamura M (1995) Continuous mixing of crystal mush and replenished magma in the
1113 ongoing Unzen eruption. Geology 23:807–810. doi: 10.1130/0091-
1114 7613(1995)023<0807:CMOCMA>2.3.CO;2

1115 Neave DA, Buisman I, Maclennnnan J (2017) Continuous mush disaggregation during the
1116 long-lasting Laki fissure eruption, Iceland. Am Mineral 102:2007–2021. doi:
1117 10.2138/am-2017-6015CCBY

1118 Nemeth K, Kereszturi G (2015) Monogenetic volcanism: personal views and discussion. Int J
1119 Earth Sci 104:2131–2146. doi: 10.1007/s00531-015-1243-6

1120 Nishimura K, Kawamoto T, Kobayashi T, et al (2005) Melt inclusion analysis of the Unzen
1121 1991-1995 dacite: implications for crystallization processes of dacite magma. Bull
1122 Volcanol 67:648–662. doi: 10.1007/s00445-004-0400-8

1123 Ozawa A, Tagami T, Kamata H (2006) Argon isotopic composition of some Hawaiian historical
1124 lavas. Chem Geol 226:66–72. doi: 10.1016/j.chemgeo.2005.10.001

1125 Pécskay Z, Lexa J, Szakacs A, et al (1995) Space and time distribution of Neogene-Quaternary
1126 volcanism in the Carpatho- Pannonian Region. Acta Vulcanol 7:15–28

1127 Pécskay Z, Lexa J, Szakacs A, et al (2006) Geochronology of Neogene magmatism in the
1128 Carpathian arc and intra-Carpathian area. Geol Carpathica 57:511–530

1129 Pécskay Z, Szakács A, Seghedi I, Karátson D (1992) New data on the geochronological
1130 interpretation of Cucu volcano and its environs (South Harghita, Romania). Hung
1131 Földt Közl 122/2–4:265–286

1132 Peltz S, Vajdea E, Balogh K, Pécskay Z (1987) Contribution to the geochronological study of
1133 the volcanic processes in the Calimani and Harghita Mts. In: Contribution to the
1134 geochronological study of the volcanic processes in the Calimani and Harghita Mts.
1135 Dari S. Sed. Inst. Geol. Geofiz. Volume, pp 323–338

1136 Popa M, Radulian M, Szakács A, et al (2012) New Seismic and Tomography Data in the
1137 Southern Part of the Harghita Mountains (Romania, Southeastern Carpathians):
1138 Connection with Recent Volcanic Activity. Pure Appl Geophys 169:1557–1573. doi:
1139 10.1007/s00024-011-0428-6

1140 Quidelleur X, Gillot PY, Soler V, Lefevre JC (2001) K/Ar dating extended into the last
1141 millennium: application to the youngest effusive episode of the Teide volcano
1142 (Spain). Geophys Res Lett 28:3067–3070. doi: 10.1029/2000GL012821

1143 Rangel E, Arce JL, Macias JL (2018) Storage conditions of the similar to 29 ka rhyolitic
1144 Guangoche White Pumice Sequence, Los Azufres Volcanic Field, Central Mexico. J
1145 Volcanol Geotherm Res 358:132–148. doi: 10.1016/j.jvolgeores.2018.03.016

1146 Reid MR, Vazquez JA, Schmitt AK (2011) Zircon-scale insights into the history of a
1147 Supervolcano, Bishop Tuff, Long Valley, California, with implications for the Ti-in-
1148 zircon geothermometer. Contrib Mineral Petrol 161:293–311. doi: 10.1007/s00410-
1149 010-0532-0

1150 Reyes-Guzman N, Siebe C, Chevrel MO, et al (2018) Geology and radiometric dating of
1151 Quaternary monogenetic volcanism in the western Zacapu lacustrine basin
1152 (Michoacan, Mexico): implications for archeology and future hazard evaluations. Bull
1153 Volcanol 80:18. doi: 10.1007/s00445-018-1193-5

1154 Rubin A, Cooper KM, Leever M, et al (2016) Changes in magma storage conditions following
1155 caldera collapse at Okataina Volcanic Center, New Zealand. Contrib Mineral Petrol
1156 171:4. doi: 10.1007/s00410-015-1216-6

1157 Samper A, Quidelleur X, Komorowski J-C, et al (2009) Effusive history of the Grande
1158 Decouverte Volcanic Complex, southern Basse-Terre (Guadeloupe, French West
1159 Indies) from new K-Ar Cassignol-Gillot ages. J Volcanol Geotherm Res 187:117–130.
1160 doi: 10.1016/j.jvolgeores.2009.08.016

1161 Samper A, Quidelleur X, Lahitte P, Mollex D (2007) Timing of effusive volcanism and collapse
1162 events within an oceanic arc island: Basse-Terre, Guadeloupe archipelago (Lesser
1163 Antilles Arc). Earth Planet Sci Lett 258:175–191. doi: 10.1016/j.epsl.2007.03.030

1164 Schimmelpfennig I, Benedetti L, Garreta V, et al (2011) Calibration of cosmogenic Cl-36
1165 production rates from Ca and K spallation in lava flows from Mt. Etna (38 degrees N,
1166 Italy) and Payun Matru (36 degrees S, Argentina). Geochim Cosmochim Acta
1167 75:2611–2632. doi: 10.1016/j.gca.2011.02.013

1168 Schmitt AK, Stockli DF, Niedermann S, et al (2010) Eruption ages of Las Tres Virgenes volcano
1169 (Baja California): A tale of two helium isotopes. Quat Geochronol 5:503–511. doi:
1170 10.1016/j.quageo.2010.02.004

1171 Seghedi I, Matenco L, Downes H, et al (2011) Tectonic significance of changes in post-
1172 subduction Pliocene-Quaternary magmatism in the south east part of the Carpathian-
1173 Pannonian Region. Tectonophysics 502:146–157. doi: 10.1016/j.tecto.2009.12.003

1174 Shane P, Martin SB, Smith VC, et al (2007) Multiple rhyolite magmas and basalt injection in
1175 the 17.7 ka Rerewhakaaitu eruption episode from Tarawera volcanic complex, New
1176 Zealand. J Volcanol Geotherm Res 164:1–26. doi: 10.1016/j.jvolgeores.2007.04.003

1177 Singer BS, Thompson RA, Dungan MA, et al (1997) Volcanism and erosion during the past
1178 930 ky at the Tatara San Pedro complex, Chilean Andes. Geol Soc Am Bull 109:127–
1179 142. doi: 10.1130/0016-7606(1997)109<0127:VAEDTP>2.3.CO;2

1180 Singer BS, Wijbrans JR, Nelson ST, et al (1998) Inherited argon in a Pleistocene andesite lava:
1181 40Ar/39Ar incremental-heating and laser-fusion analyses of plagioclase. Geology
1182 26:427–430

1183 Smith VC, Shane P, Nairn IA (2004) Reactivation of a rhyolitic magma body by new rhyolitic
1184 intrusion before the 15.8 ka Rotorua eruptive episode: implications for magma
1185 storage in the Okataina Volcanic Centre, New Zealand. J Geol Soc 161:757–772. doi:
1186 10.1144/0016-764903-092

1187 Smith VC, Shane P, Nairn IA (2005) Trends in rhyolite geochemistry, mineralogy, and magma
1188 storage during the last 50 kyr at Okataina and Taupo volcanic centres, Taupo Volcanic
1189 Zone, New Zealand. J Volcanol Geotherm Res 148:372–406. doi:
1190 10.1016/j.jvolgeores.2005.05.005

1191 Steiger R, Jager E (1977) Subcommission on geochronology - convention on use of decay
1192 constants in geochronology and cosmochronology. Earth Planet Sci Lett 36:359–362.
1193 doi: 10.1016/0012-821X(77)90060-7

1194 Stewart RB (2010) Andesites as Magmatic Liquids or Liquid-crystal Mixtures; Insights from
1195 Egmont and Ruapehu Volcanoes, New Zealand. Cent Eur J Geosci 2:329–338. doi:
1196 10.2478/v10085-010-0022-7

1197 Stipp J, Mcdougal I, Polach H (1969) Excess radiogenic argon in young subaerial basalts from
1198 Auckland volcanic field New Zealand. Trans-Am Geophys Union 50:330-+

1199 Szabo C, Harangi S, Csontos L (1992) Review Of Neogene And Quaternary Volcanism Of The
1200 Carpathian Pannonian Region. Tectonophysics 208:243–256. doi: 10.1016/0040-
1201 1951(92)90347-9

1202 Szakács A, Seghedi I (1995) The Călimani–Gurghiu–Harghita volcanic chain, East Carpathians,
1203 Romania: volcanological features. Acta Volcanol 7:145–153

1204 Szakács A, Seghedi I, Pécskay Z (1993) Peculiarities of South Harghita Mts. as terminal
1205 segment of the Carpathian Neogene to Quaternary volcanic chain. Rev Roum Géol
1206 Géophys Géogr Géol 37:21–37

1207 Szakács A, Seghedi I, Pécskay Z, Mirea V (2015) Eruptive history of a low-frequency and low-
1208 output rate Pleistocene volcano, Ciomadul, South Harghita Mts., Romania. Bull
1209 Volcanol 77:. doi: 10.1007/s00445-014-0894-7

1210 Tanaka K, Shoemaker E, Ulrich G, Wolfe E (1986) Migration of volcanism in the San-Francisco
1211 volcanic field, Arizona. Geol Soc Am Bull 97:129–141. doi: 10.1130/0016-
1212 7606(1986)97<129:MOVITS>2.0.CO;2

1213 Tantau I, Reille M, de Beaulieu JL, et al (2003) Vegetation history in the Eastern Romanian
1214 Carpathians: pollen analysis of two sequences from the Mohos crater. Veg Hist
1215 Archaeobotany 12:113–125. doi: 10.1007/s00334-003-0015-6

1216 Torres-Orozco R, Arce JL, Layer PW, Benowitz JA (2017) The Quaternary history of effusive
1217 volcanism of the Nevado de Toluca area, Central Mexico. J South Am Earth Sci 79:12–
1218 39. doi: 10.1016/j.jsames.2017.07.008

Turner MB, Bebbington MS, Cronin SJ, Stewart RB (2009) Merging eruption datasets: building an integrated Holocene eruptive record for Mt Taranaki, New Zealand. Bull Volcanol 71:903–918. doi: 10.1007/s00445-009-0274-x

Turner MB, Cronin SJ, Bebbington MS, et al (2011) Integrating records of explosive and effusive activity from proximal and distal sequences: Mt. Taranaki, New Zealand. Quat Int 246:364–373. doi: 10.1016/j.quaint.2011.07.006

Vaselli O, Minissale A, Tassi F, et al (2002) A geochemical traverse across the Eastern Carpathians (Romania): constraints on the origin and evolution of the mineral water and gas discharges. Chem Geol 182:637–654. doi: 10.1016/S0009-2541(01)00348-5

Vinkler A, Harangi S, Ntaflos T, Szakács A (2007) Petrology and geochemistry of pumices from the Ciomadul volcano (Eastern Carpathians)—implication for petrogenetic processes. (in Hungarian with an English abstract). Foldtani Kozlony 103–128

Wulf S, Fedorowicz S, Veres D, et al (2016) The “Roxolany Tephra’’ (Ukraine) - new evidence for an origin from Ciomadul volcano, East Carpathians.” J Quat Sci 31:565–576. doi: 10.1002/jqs.2879

Zellmer G, Turner S, Hawkesworth C (2000) Timescales of destructive plate margin magmatism: new insights from Santorini, Aegean volcanic arc. Earth Planet Sci Lett 174:265–281. doi: 10.1016/S0012-821X(99)00266-6

Zellmer GF, Sparks RSJ, Hawkesworth CJ, Wiedenbeck M (2003) Magma emplacement and remobilization timescales beneath Montserrat: Insights from Sr and Ba zonation in plagioclase phenocrysts. J Petrol 44:1413–1431. doi: 10.1093/petrology/44.8.1413

Zimmerer MJ, Lafferty J, Coble MA (2016) The eruptive and magmatic history of the youngest pulse of volcanism at the Valles caldera: Implications for successfully dating late Quaternary eruptions. J Volcanol Geotherm Res 310:50–57. doi: 10.1016/j.jvolgeores.2015.11.021

Figure captions

Fig. 1 A) DEM in shaded relief of Eastern Carpathian; B) Location of the main East Carpathian volcanic massifs; C) Ciomadul dome complex. Sample locations (squares) are color-coded according to their sector: red squares: peripheral south-eastern and northern domes; green squares: western-central part of the dome complex; purple squares: eastern-central part of the dome complex. Ages and uncertainties are in ka. St. Ana and Mohoş: uneroded twin craters.

Fig. 2 Photomicrograph of a thin section of the Haramul Mare dome in plane-polarised (A) and cross-polarised (B) view. Plag.: plagioclase; Biot.: biotite; Amp.: amphibole; Glom.: glomerocrysts, mostly composed of plagioclase phenocrysts and small hornblende (Hb.), appear in the upper part as a crystal clot. Width is 10 mm. C) Close-up view of the microlitic groundmass and microphenocrysts.

Fig. 3 Illustration of the procedure of the two-step sample separation from a photomicrograph of sample 15CIO01. Mosaics b, c and d simulate the results of the separation. Each square in these mosaics represents a fraction of the crushed sample that is either kept (visible) or removed (hidden by green squares) during the separation. a) Thin section in cross-polarised light (field of view is 8 mm wide). Labels highlight characteristic anhedral glomerocryst (anh. glom.) and euhedral plagioclase (enh. plag.). b) Grains selected by the first step. Note the small diamond-like phenocryst (at the center left), the peripheral part of large phenocrysts, and the abundance of microphenocrysts (in the upper half) that remain after this first step. c) Grains that remain selected after the second step of

1267 preparation. d) Grains that would not be removed from the groundmass in the case of a
1268 single-step of separation.

1269 Fig. 4 Semi-log crystal size distribution (CSD) plots for mineral phases in the Ciomadul lava
1270 dome A) Plagioclase (black curves) and mafic (amphibole and biotite, grey curves) crystal
1271 CSD plot. All but those for sample 16CIO08 (coloured curves) show kinked profiles. Insets
1272 show analysed micro-photographs used in the CSD plots in B) and C) (plagioclase in white,
1273 mafic crystals in black, groundmass in grey) B) Fitting of a mixture of two magmas with linear
1274 CSDs to the observed CSD from samples 16CIO01 and 15CIO09 for plagioclases focussed on
1275 the kink zone between the two linear segments for the fine and coarse grains. Regressions
1276 though coherent populations, for which assumptions of near-uniform morphologies are
1277 valid, are shown as dotted lines. Values for the equation of these regressed lines and R^2
1278 values are given (same box colour as the corresponding line). Inset shows the complete CSD
1279 graph. C) Same graph as B) but for mafic (biotite) crystals.

1280 Fig. 5 Graph comparing K-Ar results and those proposed in previous studies. Each dome on
1281 this diagram is plotted according to the age obtained by this work (X-axis) vs. the age
1282 obtained in previous studies (Y-axis). Error bars and black squares show 2σ (95%) confidence
1283 interval.

1284 Fig. 6 A) K_2O vs SiO_2 diagram (Peccerillo and Taylor; 1976), for Ciomadul lava dome samples;
1285 B) Harker diagrams showing the variations of major element oxides as a function of SiO_2.

1286 Fig. 7 Whole-rock age model from thin section analysis (sample 15CIO01, same as Fig. 3). a)
1287 Upper left: Identification of the mineral phases by binarization; lower right: Mosaicing of
1288 previous image to simulate 200 μm grain size. b) Grain composition analysis from their
1289 grayscale properties (converted to colour for easier identification). Yellow: pure plagioclase;

1290 blue: groundmass; shaded white to red to black: mixed grains with increasing proportion of
1291 groundmass grains. c) Distribution of the grain density proportion (left Y-axis) and ages
1292 modelled for each grain composition (dotted black curve scaled on the right Y-axis). Bottom
1293 scale defines the expected density of the respective grain populations.

1294 Fig. 8 Graph of the inherited argon abundance (deduced from whole-rock ages) versus
1295 abundance of glomerocrysts (in vol%). Heavy lines display a ± 1σ correlation trend. Thin
1296 horizontal lines are the estimation (± 1σ) of inherited argon abundance for the Dealul Cetăţii
1297 dome obtained from the analysis of its thin section in order to propose a corrected eruption
1298 age.

1299 Fig. 9 Compilation of the ages obtained on groundmass and separated minerals. Samples are
1300 sorted with respect to the distance to the ~2 Ma old Pilişca volcano.

1301 Fig. 10 Map of the ages (in ka) obtained from the different phases of the Dealul Cetăţii dome
1302 (15CIO01). The small and large grids correspond to the two-step and single-step procedure,
1303 respectively.

1304 Fig. 11 Graph of the evolution of abundance of phenocrysts, glomerocrysts (in vol% of dome,
1305 on left axis) and amount of argon inherited from xenocrysts (in %, on right axis) versus
1306 eruption age. Boxes show global trends for each parameter. Schematic cartoon summarizing
1307 a scenario for the assimilation of xenocrysts by dacitic magma based on crystal mush
1308 disaggregation and increasing incorporation of inherited crystals in juvenile magma trough
1309 time (modified from Neave et al., 2017). The figures are not to scale.

1310 Fig. 12 Geochemical evolution of major element oxides (in wt. %) of dacitic domes of
1311 Ciomadul through time (eruption ages in ka).

Table 1 CSD input parameters and results, including crystal habit and L_{max}.

Sample	Mineral	Count	Crystal Habit				Shape	L_{max}	Phase
			Short	Interm.	Long	R^2 values		(mm)	proportion
16CIO08	Plagioclase	8164	1	1.5	3	0.86	Tabular	2.93	35.2%
16CIO08	Mafic m.	5454	1	1.5	3	0.85	Columnar	1.58	12.3%
15CIO01	Plagioclase	3465	1	1.3	2.1	0.88	Tabular	4.20	29.5%
15CIO01	Mafic m.	2781	1	1.25	2.1	0.83	Columnar	1.39	7.9%
15CIO09	Plagioclase	5720	1	1.25	2.1	0.86	Tabular	4.79	38.0%
15CIO09	Mafic m.	2008	1	1.5	3	0.88	Columnar	2.08	11.3%
16CIO09	Plagioclase	3020	1	1.3	2.2	0.87	Tabular	4.31	33.7%
16CIO09	Mafic m.	3486	1	1.6	2.9	0.88	Columnar	1.55	7.4%

Table_02

Table 2 K-Ar ages obtained in this study for Ciomadul lava domes. (G.M.: groundmass; : Plag. µP.: plagioclase microphenocrysts; D.S.: two-step separation; S.S.: single-step separation); Sample coordinates are projected using the Universal Transverse Mercator (UTM) projection (zone 35 N).

stage	Sample code Dome Name	Easting (in m)	Northing (in m)	Elevation (m asl)	Dated phase	Fraction Size (µm)	K%	^{40}Ar* ± 1σ (in % of total ^{40}Ar)		^{40}Ar* relative uncertainty	^{40}Ar* ± 1σ ×10^{11} at/g		Age ± 1σ (in ka)		Weighted mean age ± 1σ
1st stage	16CIO08	418645	5107909	1099	G.M.	63-125	3.226	5.233	0.169	0.726%	23.29	0.885	691	17	
	Muntele Puturosu							4.489	0.108	0.446%	24.26	0.485	720	19	**704 ± 18**
	16CIO07	419620	5107472	846	G.M.	63-125	3.585	29.213	0.089	0.373%	23.78	2.592	635	10	
	Balvanyos							34.293	0.065	0.268%	24.19	2.225	646	9	**641 ± 9**
	16CIO06	419673	5107443	856	G.M.	63-125	3.449	4.283	0.043	0.280%	15.45	0.185	429	12	
	Balvanyos							4.488	0.101	0.624%	16.24	0.455	451	12	**440 ± 12**
2nd stage	16CIO01	416986	5114107	866	Plag. µP.	63-125	1.336	1.025	0.201	6.438%	3.127	0.206	224	26	
	Haramul Mic							1.211	0.076	2.065%	3.680	0.092	264	23	**245 ± 24**
	15CIO01	413713	5110905	994	G.M.	63-125	3.722	4.399	0.084	1.182%	7.139	0.371	184	5	
	Dealul Cetăţii							4.170	0.075	1.055%	7.132	0.314	183	5	**184 ± 5**
	16CIO02	413146	5109912	1242	G.M.	63-125	3.471	4.266	0.055	1.055%	5.220	0.235	144	4	
	Vârful Comlos							4.234	0.016	0.307%	5.209	0.068	144	4	**144 ± 4**
	16CIO04	413873	5109760	1260	Plag. µP.	40-80	1.391	1.209	0.029	1.655%	1.725	0.034	119	10	
	Ciomadul Mare							1.508	0.049	2.322%	2.102	0.074	145	10	**133 ± 18**
	15CIO09	416664	5111953	902	G.M.	63-125	3.668	6.414	0.042	1.107%	3.754	0.267	98	2	
	Haramul Mare							12.020	0.073	2.005%	3.639	0.877	95	2	**96 ± 2**
	16CIO09	415362	5108313	1101	G.M.	63-125	3.441	1.162	0.058	2.840%	2.042	0.067	57	5	
	Piscul Pietros							1.323	0.063	2.797%	2.239	0.083	62	5	**60 ± 5**

1015 Table 3 Major element concentrations for the Ciomadul lava domes (in wt%%).

Sample	15CIO09	16CIO01	16CIO02	16CIO03	16CIO04	16CIO05	16CIO06	16CIO07	16CIO08	16CIO09	16CIO11
SiO2	65.26	66.18	66.59	65.60	66.87	66.50	61.80	61.74	64.68	67.07	67.36
TiO2	0.45	0.35	0.38	0.37	0.32	0.32	0.52	0.53	0.53	0.31	0.29
Al2O3	16.85	16.46	16.62	16.62	16.29	16.20	17.35	17.43	17.82	16.15	16.26
Fe2O3	2.86	2.41	2.47	2.51	2.28	2.28	3.54	3.65	2.22	2.11	1.99
MnO	0.06	0.05	0.05	0.05	0.05	0.05	0.07	0.07	0.04	0.05	0.04
MgO	1.93	1.54	1.64	1.67	1.52	1.51	2.18	2.22	1.33	1.39	1.32
CaO	4.03	3.55	3.66	3.65	3.22	3.26	4.78	4.94	3.56	3.00	2.89
Na2O	4.34	4.07	4.34	4.24	4.30	4.31	4.22	4.33	4.36	4.43	4.67
K2O	3.36	3.46	3.32	3.21	3.61	3.57	3.40	3.20	3.28	3.55	3.50
P2O5	0.20	0.12	0.16	0.14	0.13	0.14	0.18	0.18	0.13	0.11	0.12
LOI	0.3	1.5	0.4	1.6	1.1	1.5	1.6	1.3	1.6	1.5	1.2
Sum	99.64	99.69	99.63	99.66	99.69	99.64	99.64	99.59	99.55	99.67	99.64

1016

Table_04

Table 4 Comparison between new and previously proposed ages. For each dated dome, abundance (in vol%) are given for: K-bearing minerals (P.: plagioclase; B.: biotite; A.: amphibole), total of K-bearing phenocrysts (T. Ph.:); glomerocrysts (Glom.); and groundmass (G.M.);; W.-R. Age: previously proposed age on whole-rock for the same lava dome; $Ar_{inherited}$: fraction (in %) of the total of radiogenic argon assumed to be inherited; Source: references for whole rock and (U–Th)/He ages: 1: Casta (1980); 2: Pécskay et al. (1992); 3: Pécskay et al. (1995b); 4: Karátson et al., (2013); 5 : Szakács et al. (2015); 6: Harangi et al. (2015b); 7: Molnár et al. (2018); 8: this work

Location	**New measurements (this work)**								**Previously proposed ages**				
	Cassignol-Gillot (unspike) method								**Traditional K-Ar method**			**(U–Th)/He method**	
	Sample	**Phenocryst vol%**			**T. Ph.**	**Glom.**	**G.M.**	**Age**	**W.-R. age**	**Sour-**	**$Ar_{inherited}$**	**(U–Th)/He**	**Sour-**
		P.	**B.**	**A.**	**vol%**	**vol%**	**vol%**	**(in ka)**		**ce**	**(%)**	**Age**	**ce**
Puturosul	16CIO08	19	2	5	26	1	65	704 ± 18	710 ± 50	5	1 ± 7	642 ± 44	7
Bálványos	16CIO07	25	3	8	36	14	39	641 ± 9	1020 ± 150	3	37 ± 16	583 ± 30	7
Bálványos	16CIO06	23	1	7	31	13	47	440 ± 12	920 ± 180	3	52 ± 22		
Haramul Mic	16CIO01	10	2	7	19	18	54	245 ± 24	850 ± 200	1	71 ± 29	154 ± 16	7
Dealul Cetăţii	15CIO01	11	2	6	19	17	56	184 ± 5	400 ± 160	5	54 ± 45	116 – 142	4
Haramul Mare	15CIO09	12	4	6	22	16	44	96 ± 2	590 ± 160 231 ± 5	3 8	58 ± 3		
Piscul Pietros	16CIO09	21	2	8	30	23	47	60 ± 5	560 ± 110	2	89 ± 26	42.9 ± 1.5	6
Vârful Comlos	16CIO02	14	2	8	22	8	59	144 ± 4					
Ciomadul Mare	16CIO04	22	2	10	34	13	41	133 ± 18					

Table_05

1023 Table 5 K-Ar ages obtained on separated pure phases, larger grain size groundmass, and whole rock. Dated phases: Amp.: Amphibole; Biot.:

1024 Biotite; Gr.M.: groundmass; Plag. µL.: plagioclase microlites; Plag. Gl.: plagioclase glomerocrysts; W.R.: whole rock

Sample code	**Dated phase**	**Me-thod**	**Fraction Size (µm)**	**K%**	**^{40}Ar* ± 1σ (in % of total ^{40}Ar)**		**^{40}Ar* relative uncertainty**	**^{40}Ar* ± 1σ ×10^{11} at/g**		**Age ± 1σ (in ka)**		**Weighted mean age ± 1σ**	
15ClO01	Amp.	S.S.	125-250	0.931	11.113	0.030	0.270%	13.85	0.037	1423	24		
					27.431	0.153	0.558%	13.34	0.074	1371	21	**1386**	**37**
15ClO01	Plag. Gl.	S.S.	125-250	0.822	7.353	0.053	0.721%	9.72	0.070	1132	24	**1132**	**24**
15ClO01	Biot.	S.S.	125-250	6.532	20.605	0.024	0.116%	38.88	0.045	570	9		
					16.920	0.029	0.171%	38.81	0.067	569	9	**569**	**9**
15ClO01	Gr.M.	S.S.	125-250	3.612	4.039	0.038	0.941%	7.70	0.072	204	6		
					3.874	0.056	1.446%	7.52	0.109	199	7	**202**	**6**
16ClO02	Plag. Gl.	S.S.	250-500	0.655	24.750	0.087	0.352%	12.66	0.044	1848	28	**1848**	**28**
16ClO02	Plag. µL.	D.S.	63-125	0.654	7.503	0.036	0.480%	7.32	0.035	1071	21	**1071**	**21**
16ClO09	Plag. Gl.	S.S.	250-500	0.757	35.123	0.139	0.396%	7.55	0.030	955	14		
					35.222	0.114	0.324%	7.96	0.026	1007	15	**981**	**15**

16CIO09	Plag. µL.	D.S.	63-125	1.714	6.101	0.039	0.639%	3.60	0.023	201	5	**201**	**5**
16CIO09	Biot.	S.S.	125-250	6.762	8.071	0.037	0.458%	13.87	0.064	196	4	**196**	**4**
16CIO08	Plag. µL.	D.S.	63-125	1.568	4.834	0.031	0.641%	12.01	0.077	733	19		
					4.585	0.047	1.025%	12.19	0.125	744	21	**739**	**20**
16CIO04	Plag. µL.	D.S.	63-125	1.104	1.422	0.039	2.742%	1.96	0.054	170	13		
					1.523	0.042	2.758%	1.84	0.051	160	12	**165**	**12**
15CIO09	W.R.	S.S.	40-500	2.119	7.907	0.120	1.518%	5.10	0.077	230	6		
					7.874	0.036	0.457%	5.11	0.023	231	5	**231**	**5**
15CIOX2	Biot.	S.S.	125-250	5.720	3.242	0.048	1.481%	33.54	0.497	561	21	**561**	**21**

1025

Figure_01

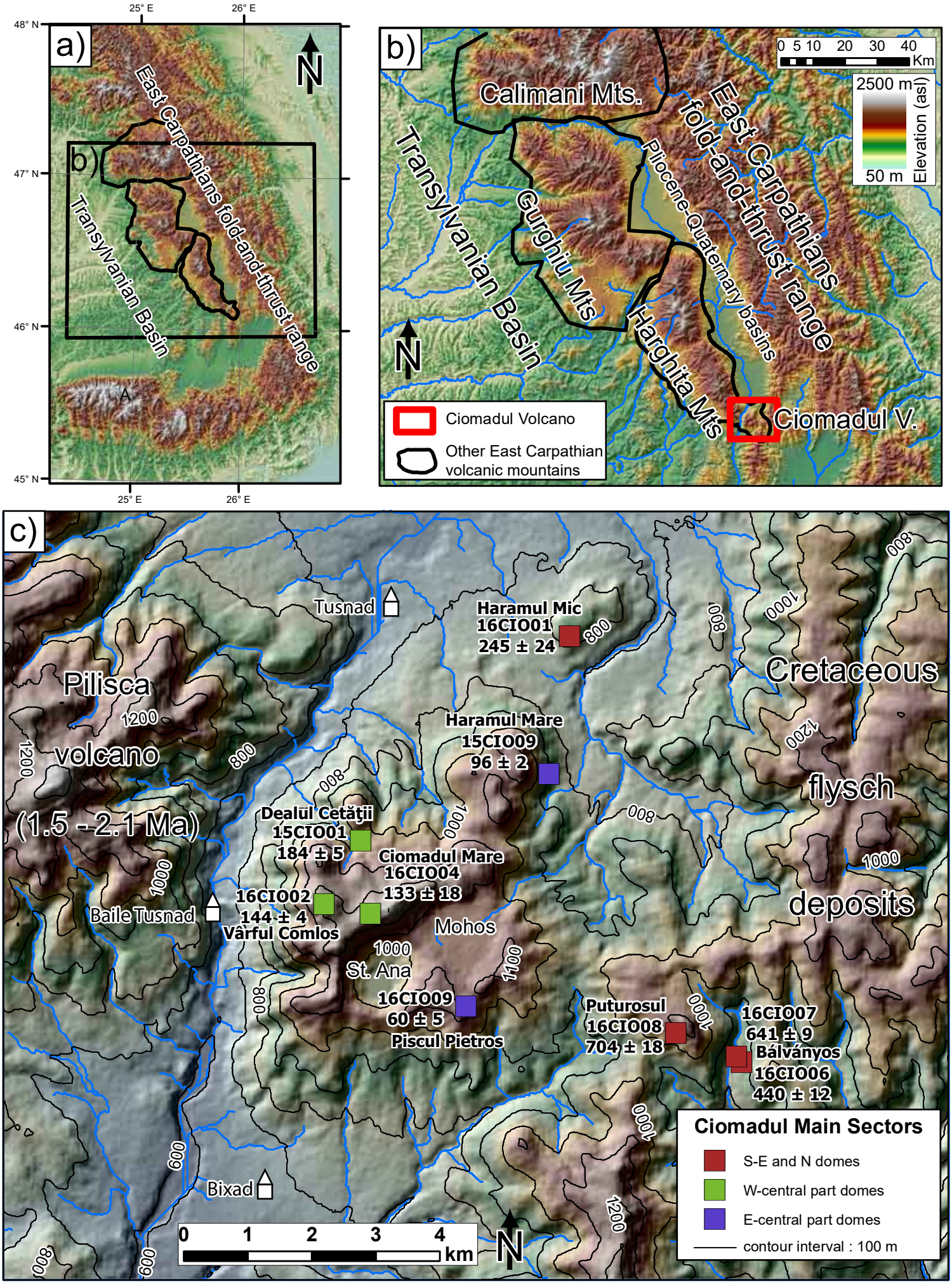
a)
b)
25° E
26° E
48° N
47° N
46° N
45° N
East Carpathians fold-and-thrust range
Transylvanian Basin
A
N
b)
0 5 10 20 30 40 Km
2500 m
50 m
Elevation (asl)
Calimani Mts.
Transylvanian Basin
Gurghiu Mts
Pliocene-Quaternary basins
East Carpathians fold-and-thrust range
Harghita Mts
Ciomadul V.
N
Ciomadul Volcano
Other East Carpathian volcanic mountains
c)
Tusnad
Haramul Mic
16CIO01
245 ± 24
Haramul Mare
15CIO09
96 ± 2
Dealul Cetăţii
15CIO01
184 ± 5
Ciomadul Mare
16CIO04
133 ± 18
16CIO02
144 ± 4
Vârful Comlos
Mohos
St. Ana
16CIO09
60 ± 5
Piscul Pietros
Puturosul
16CIO08
704 ± 18
16CIO07
641 ± 9
Bálványos
16CIO06
440 ± 12
Pilisca
volcano
(1.5 - 2.1 Ma)
Cretaceous
flysch
deposits
Baile Tusnad
Bixad
0 1 2 3 4 km
N
Ciomadul Main Sectors
S-E and N domes
W-central part domes
E-central part domes
contour interval : 100 m

Figure_02

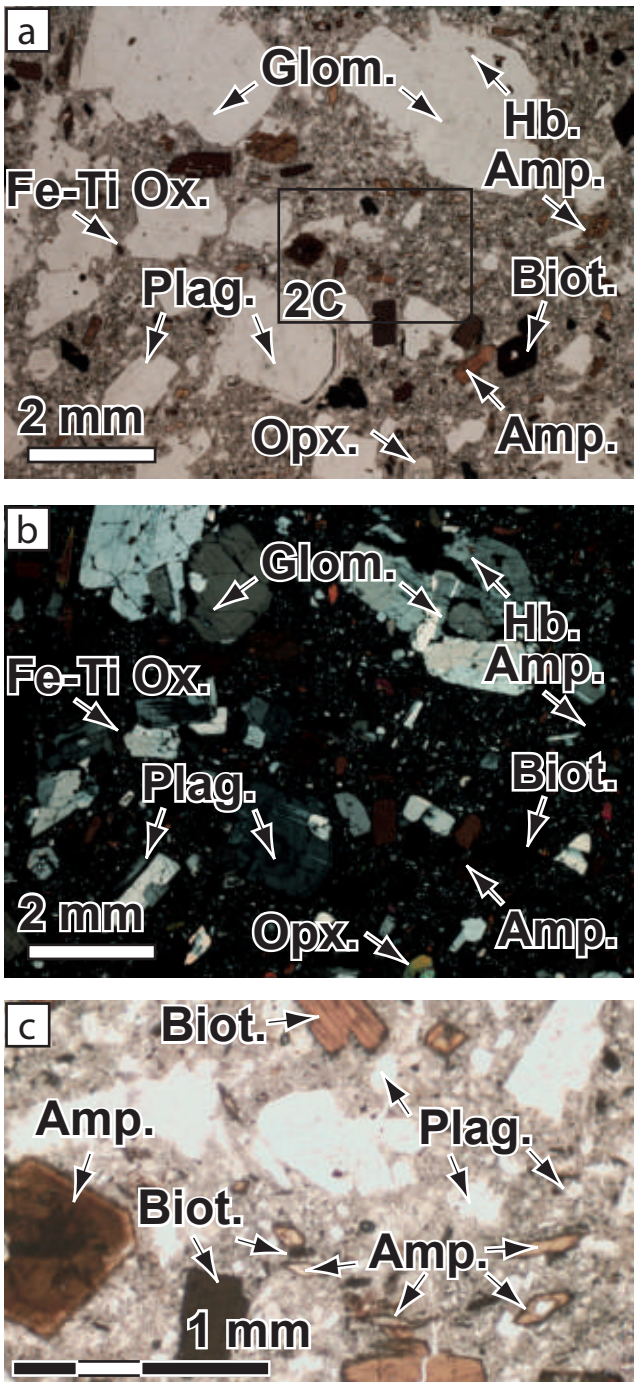
a
Glom.
Hb.
Amp.
Fe-Ti Ox.
Plag.
2C
Biot.
2 mm
Opx.
Amp.
b
Glom.
Hb.
Amp.
Fe-Ti Ox.
Plag.
Biot.
2 mm
Opx.
Amp.
c
Biot.
Amp.
Plag.
Biot.
Amp.
1 mm

Figure_03

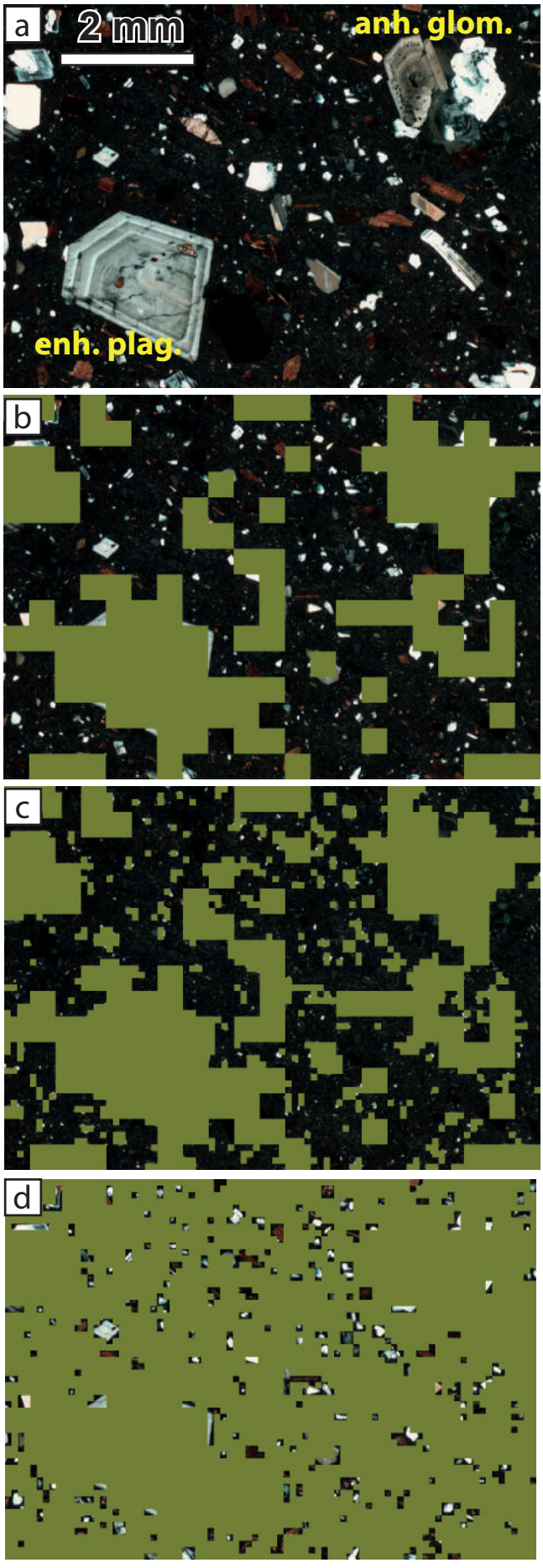

Figure_04

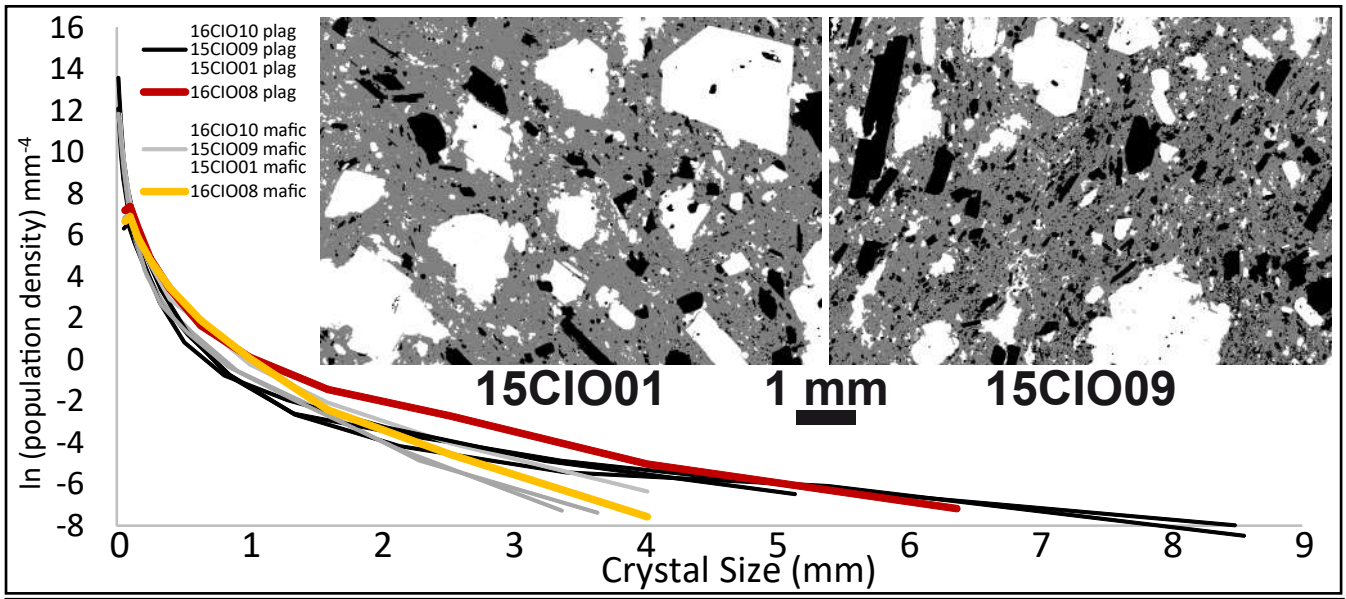
16ClO10 plag
15ClO09 plag
15ClO01 plag
16ClO08 plag
16ClO10 mafic
15ClO09 mafic
15ClO01 mafic
16ClO08 mafic
ln (population density) mm-4
Crystal Size (mm)
15ClO01
1 mm
15ClO09

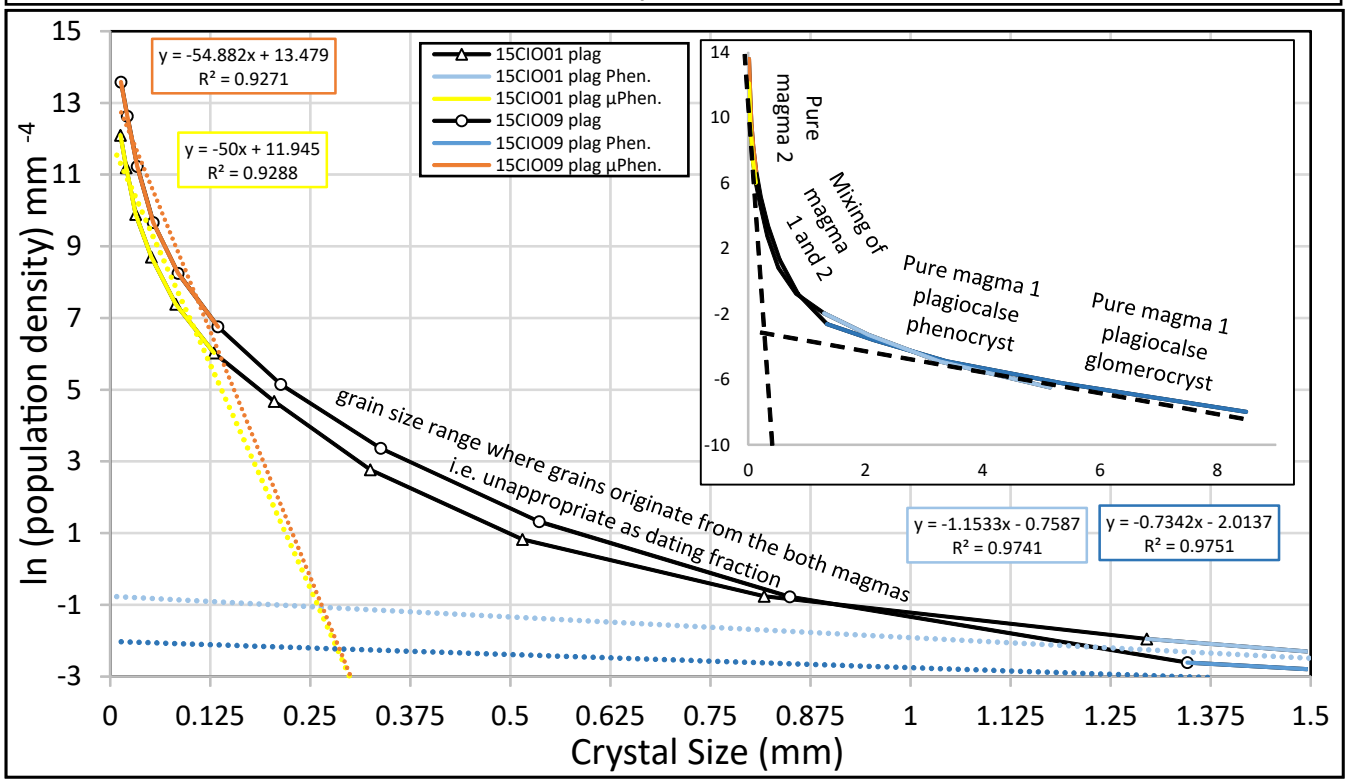
y = -54.882x + 13.479
R² = 0.9271
y = -50x + 11.945
R² = 0.9288
15ClO01 plag
15ClO01 plag Phen.
15ClO01 plag µPhen.
15ClO09 plag
15ClO09 plag Phen.
15ClO09 plag µPhen.
Pure magma 2
Mixing of magma 1 and 2
Pure magma 1 plagiocalse phenocryst
Pure magma 1 plagiocalse glomerocryst
grain size range where grains originate from the both magmas i.e. unappropriate as dating fraction
y = -1.1533x - 0.7587
R² = 0.9741
y = -0.7342x - 2.0137
R² = 0.9751
ln (population density) mm -4
Crystal Size (mm)

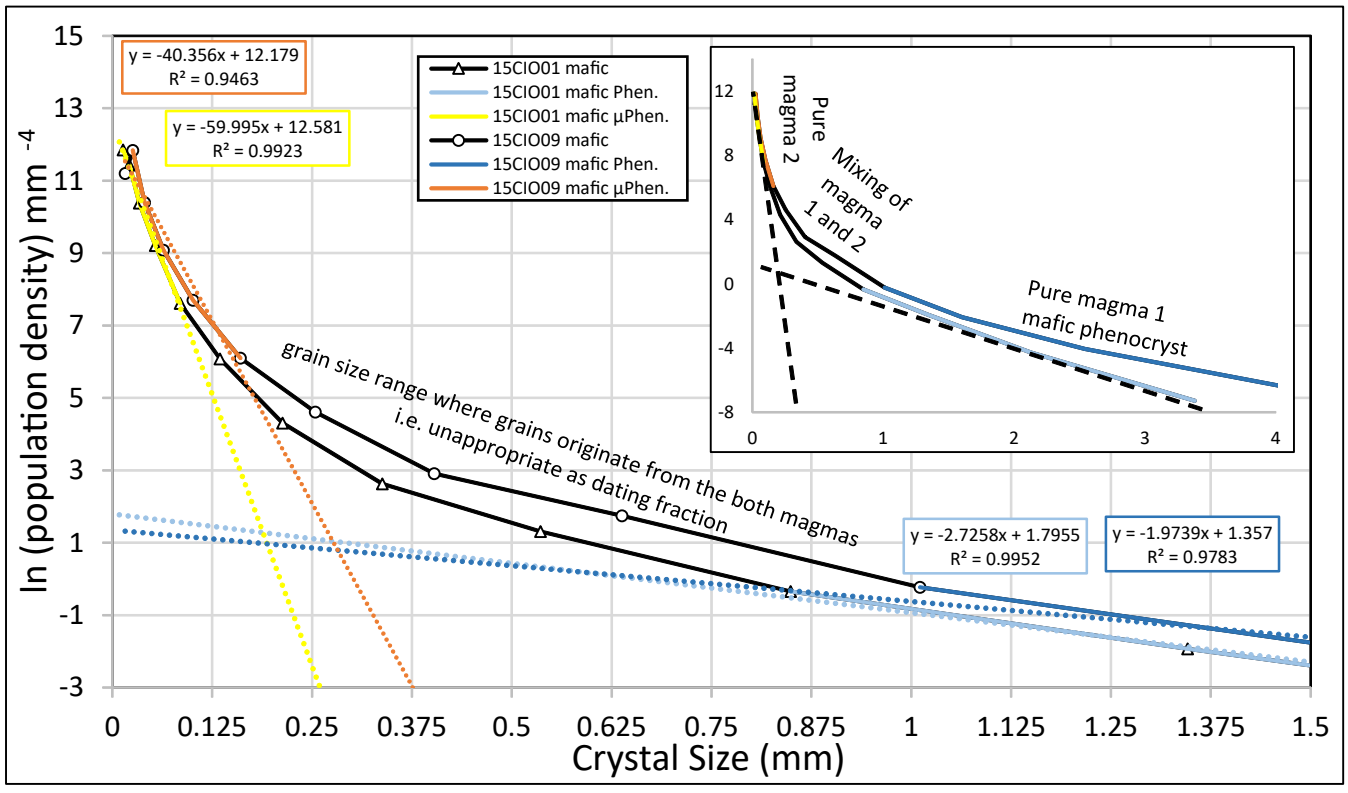
y = -40.356x + 12.179
R² = 0.9463
y = -59.995x + 12.581
R² = 0.9923
15ClO01 mafic
15ClO01 mafic Phen.
15ClO01 mafic µPhen.
15ClO09 mafic
15ClO09 mafic Phen.
15ClO09 mafic µPhen.
Pure magma 2
Mixing of magma 1 and 2
Pure magma 1 mafic phenocryst
grain size range where grains originate from the both magmas i.e. unappropriate as dating fraction
y = -2.7258x + 1.7955
R² = 0.9952
y = -1.9739x + 1.357
R² = 0.9783
ln (population density) mm -4
Crystal Size (mm)

Figure_05

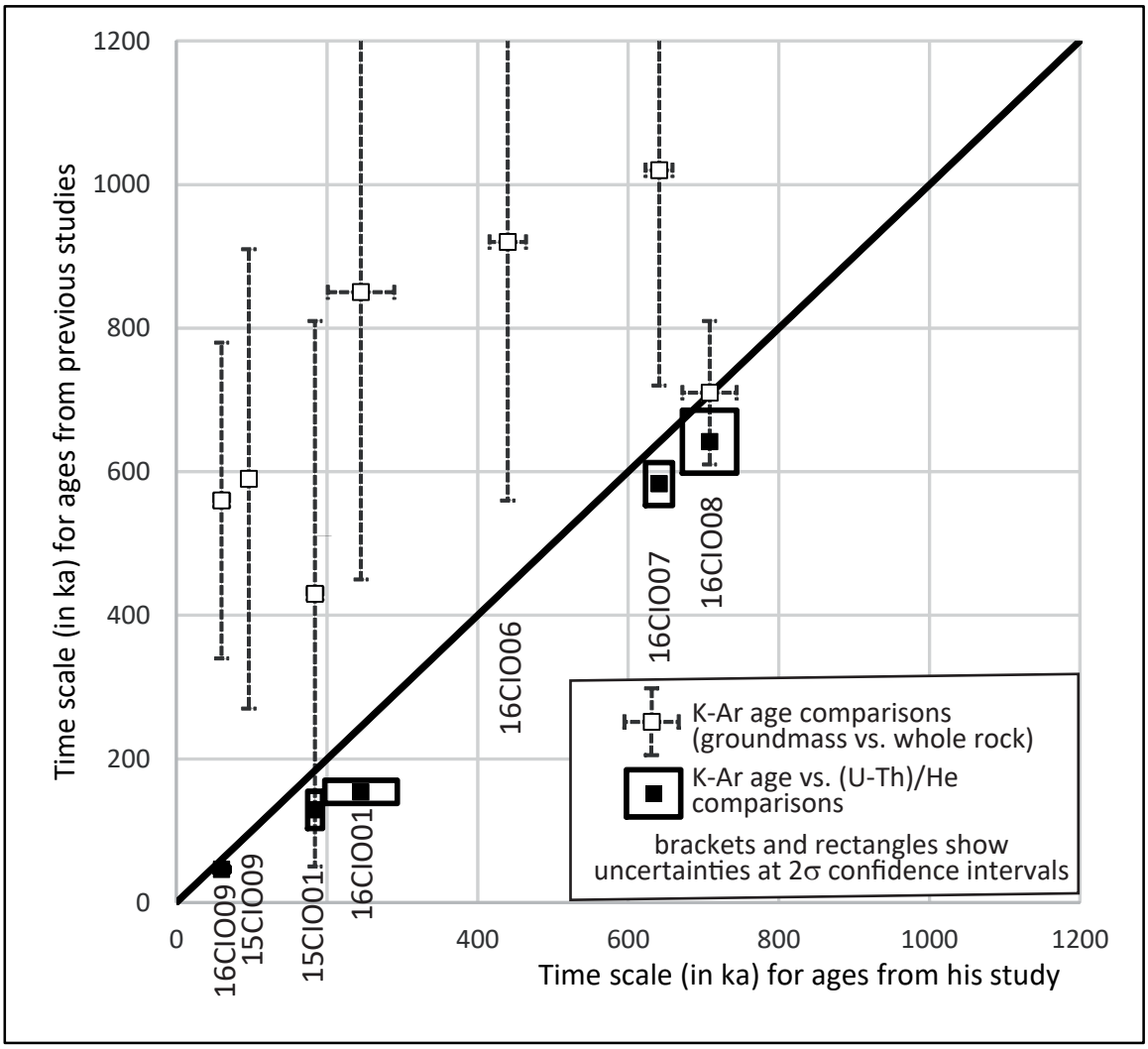
Time scale (in ka) for ages from previous studies
Time scale (in ka) for ages from his study
0
200
400
600
800
1000
1200
16CIO09
15CIO09
15CIO01
16CIO01
16CIO06
16CIO07
16CIO08
K-Ar age comparisons (groundmass vs. whole rock)
K-Ar age vs. (U-Th)/He comparisons
brackets and rectangles show uncertainties at 2σ confidence intervals

Figure_06

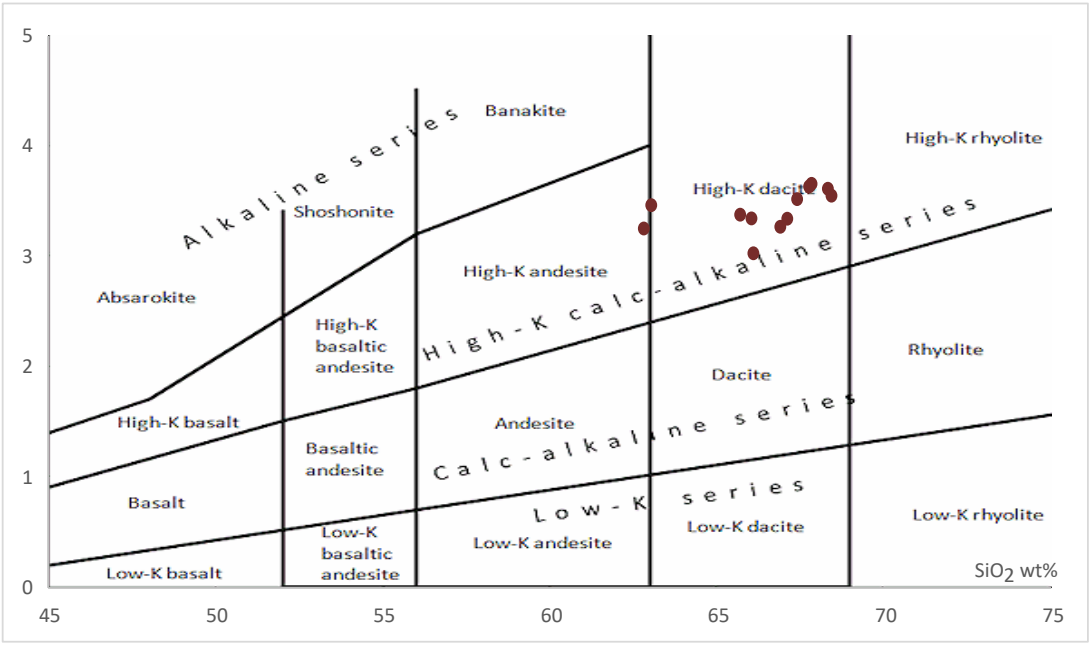
Alkaline series
Banakite
Shoshonite
Absarokite
High-K basaltic andesite
High-K andesite
High-K dacite
High-K rhyolite
High-K calc-alkaline series
Rhyolite
Dacite
High-K basalt
Basaltic andesite
Andesite
Calc-alkaline series
Basalt
Low-K series
Low-K dacite
Low-K rhyolite
Low-K basaltic andesite
Low-K andesite
Low-K basalt
SiO2 wt%
0
1
2
3
4
5
45
50
55
60
65
70
75

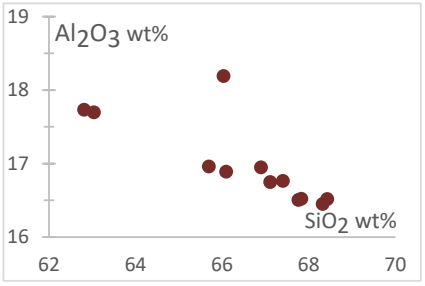
Al2O3 wt%
SiO2 wt%
16
17
18
19
62
64
66
68
70

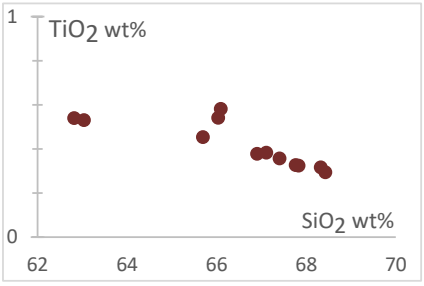
TiO2 wt%
SiO2 wt%
0
1
62
64
66
68
70

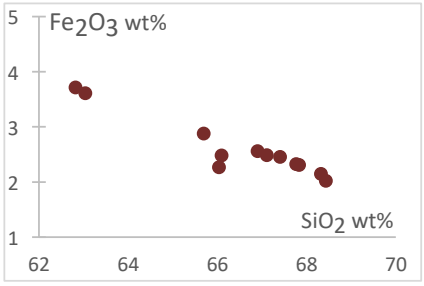
Fe2O3 wt%
SiO2 wt%
1
2
3
4
5
62
64
66
68
70

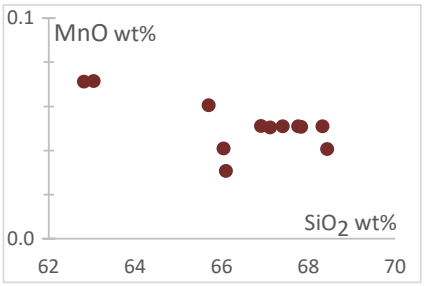
MnO wt%
SiO2 wt%
0.0
0.1
62
64
66
68
70

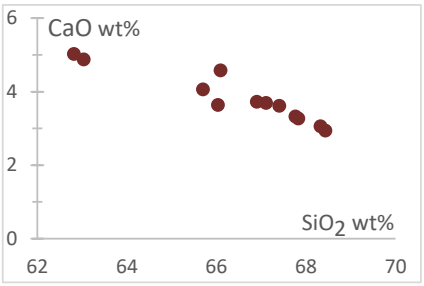
CaO wt%
SiO2 wt%
0
2
4
6
62
64
66
68
70

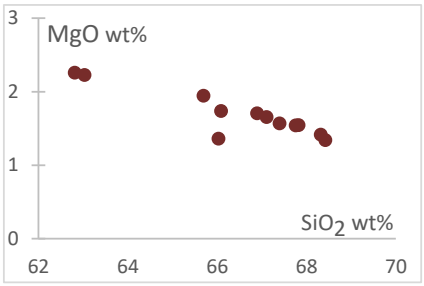
MgO wt%
SiO2 wt%
0
1
2
3
62
64
66
68
70

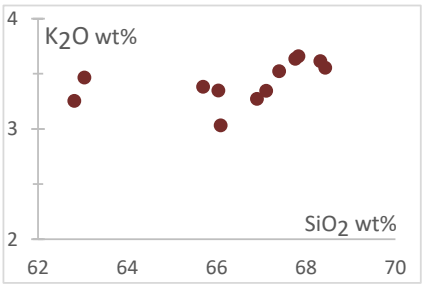
K2O wt%
SiO2 wt%
2
3
4
62
64
66
68
70

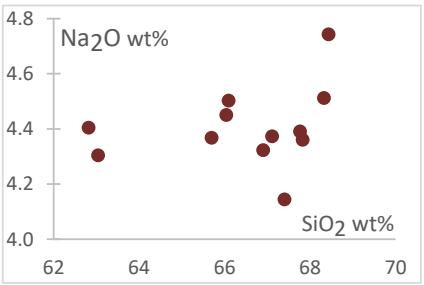
Na2O wt%
SiO2 wt%
4.0
4.2
4.4
4.6
4.8
62
64
66
68
70

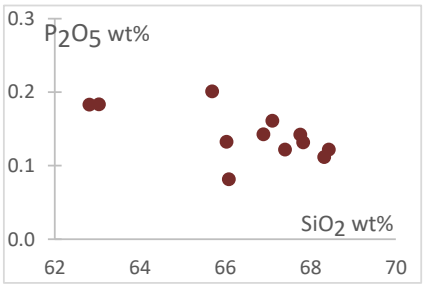
P2O5 wt%
SiO2 wt%
0.0
0.1
0.2
0.3
62
64
66
68
70

Figure_07

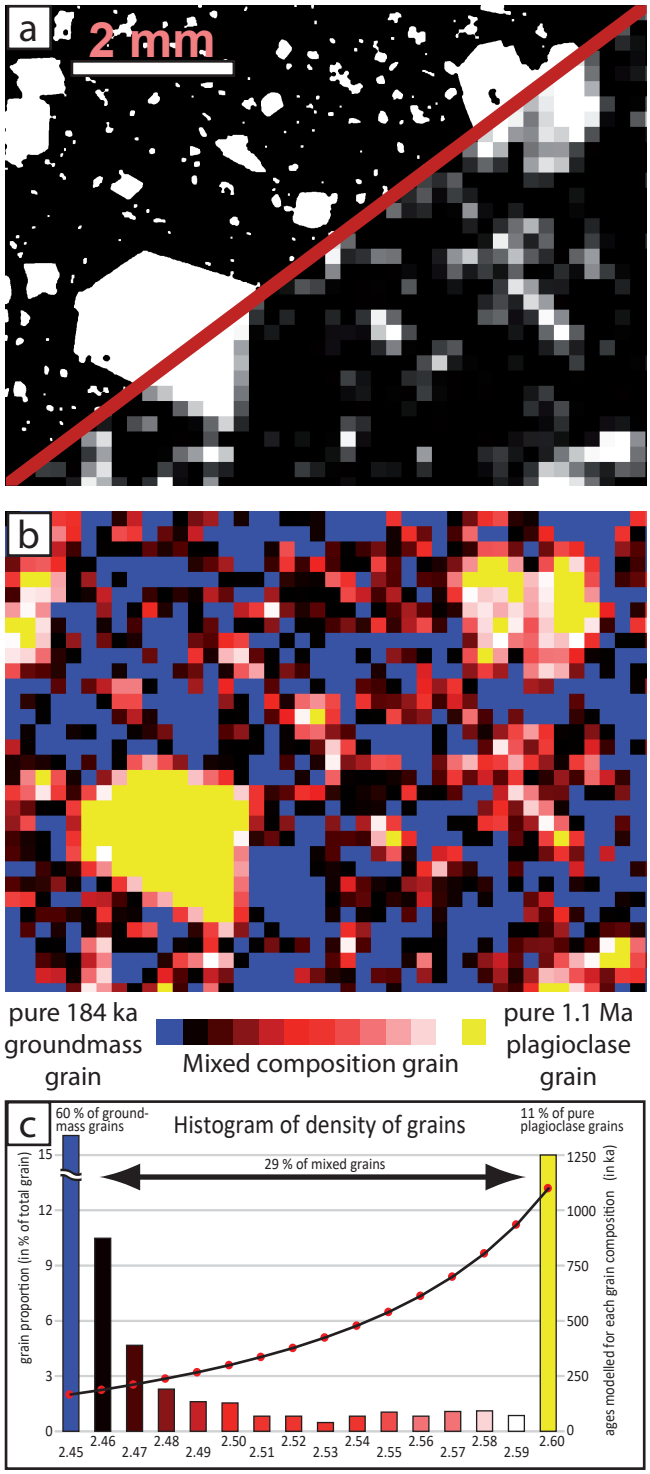
a
2 mm
b
pure 184 ka groundmass grain
Mixed composition grain
pure 1.1 Ma plagioclase grain
c
60 % of ground-mass grains
Histogram of density of grains
11 % of pure plagioclase grains
29 % of mixed grains
grain proportion (in % of total grain)
ages modelled for each grain composition (in ka)
0
3
6
9
12
15
0
250
500
750
1000
1250
2.45
2.46
2.47
2.48
2.49
2.50
2.51
2.52
2.53
2.54
2.55
2.56
2.57
2.58
2.59
2.60

Figure_08

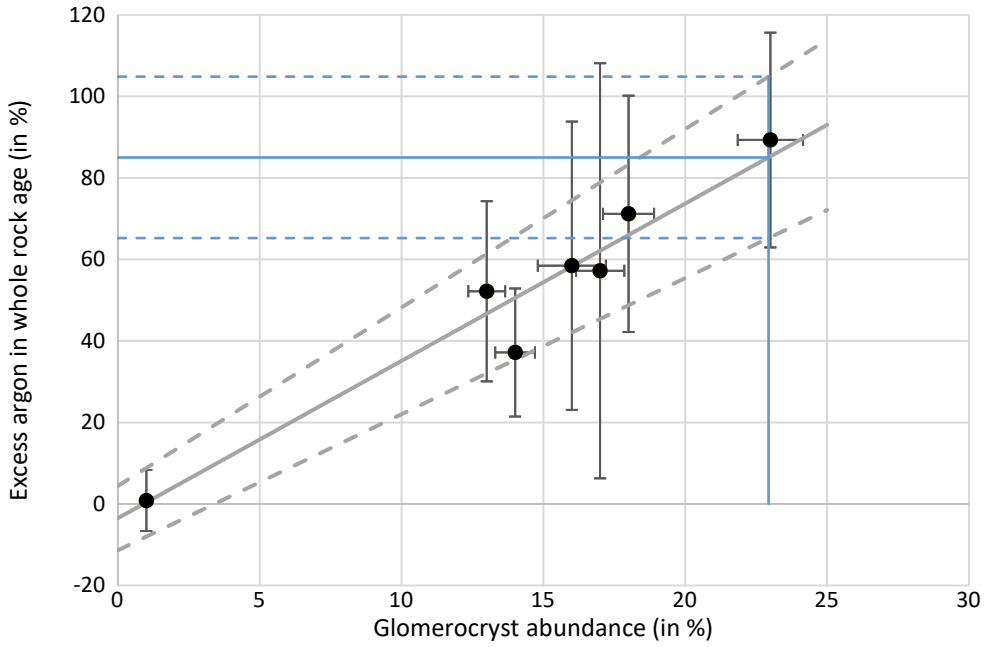
120
100
80
60
40
20
0
-20
0
5
10
15
20
25
30
Excess argon in whole rock age (in %)
Glomerocryst abundance (in %)

Figure_09

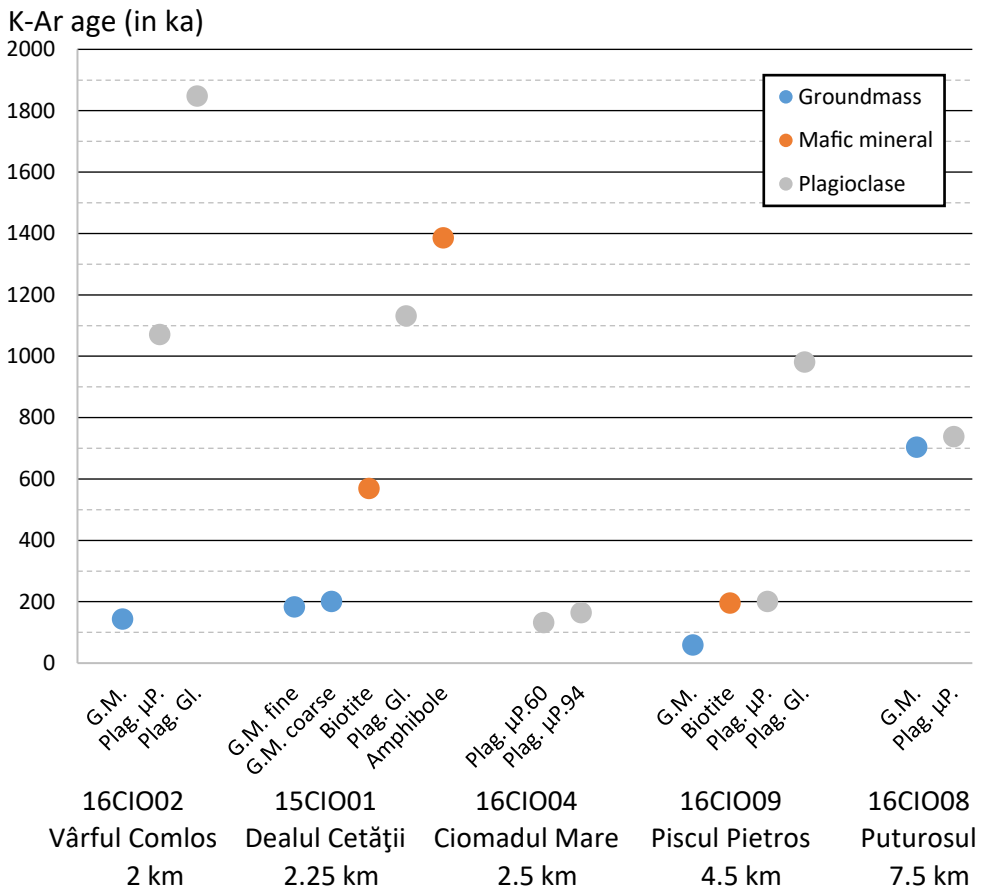
K-Ar age (in ka)
2000
1800
1600
1400
1200
1000
800
600
400
200
0
Groundmass
Mafic mineral
Plagioclase
G.M.
Plag. µP.
Plag. Gl.
G.M. fine
G.M. coarse
Biotite
Plag. Gl.
Amphibole
Plag. µP.60
Plag. µP.94
G.M.
Biotite
Plag. µP.
Plag. Gl.
G.M.
Plag. µP.
16CIO02
Vârful Comlos
2 km
15CIO01
Dealul Cetăţii
2.25 km
16CIO04
Ciomadul Mare
2.5 km
16CIO09
Piscul Pietros
4.5 km
16CIO08
Puturosul
7.5 km

Figure_10

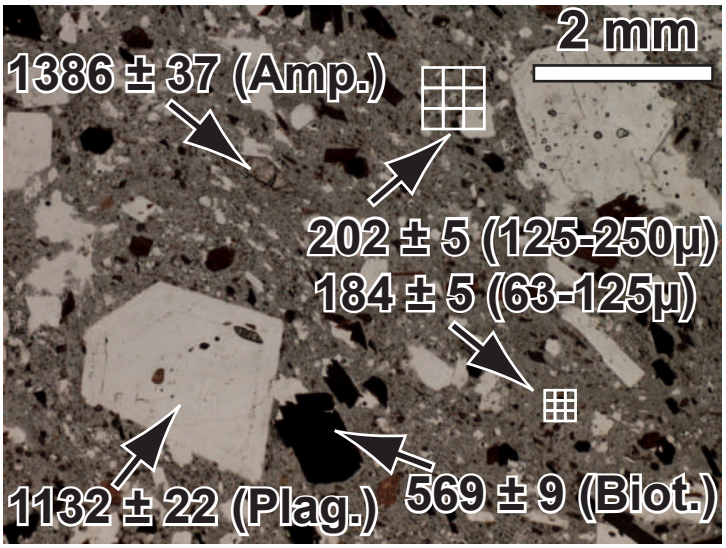
2 mm
1386 ± 37 (Amp.)
202 ± 5 (125-250µ)
184 ± 5 (63-125µ)
1132 ± 22 (Plag.)
569 ± 9 (Biot.)

Figure_11

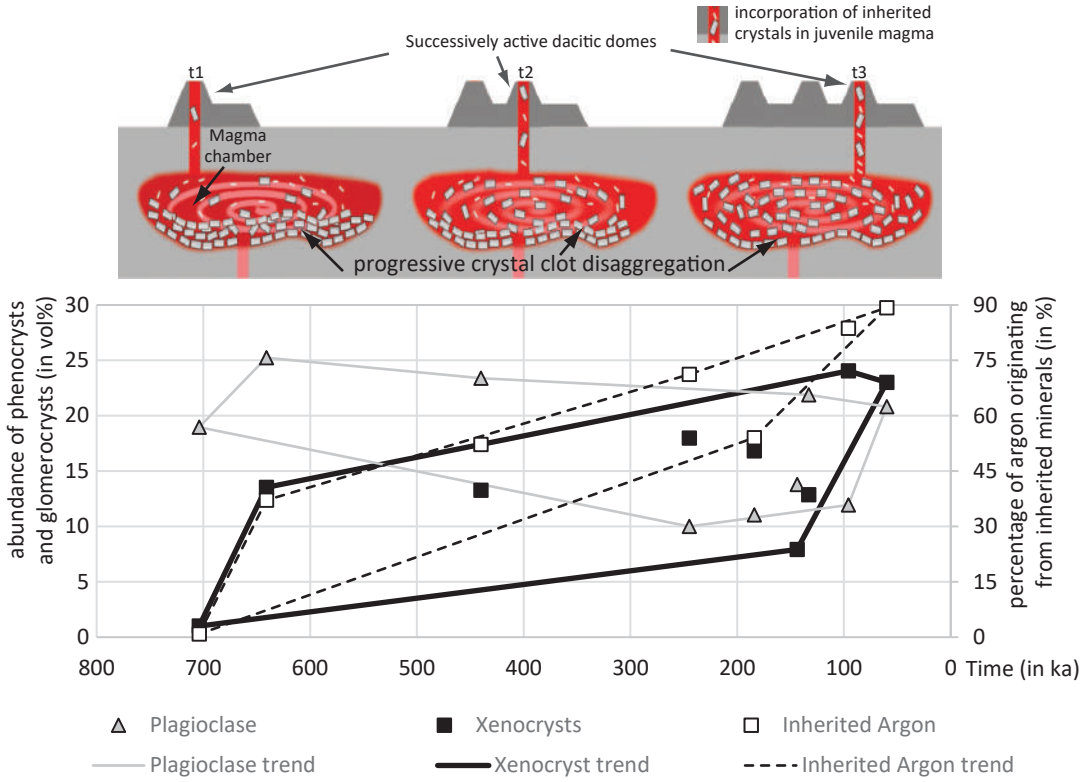
incorporation of inherited crystals in juvenile magma
Successively active dacitic domes
t1
t2
t3
Magma chamber
progressive crystal clot disaggregation
abundance of phenocrysts and glomerocrysts (in vol%)
percentage of argon originating from inherited minerals (in %)
30
25
20
15
10
5
0
90
75
60
45
30
15
0
800
700
600
500
400
300
200
100
0
Time (in ka)
Plagioclase
Xenocrysts
Inherited Argon
Plagioclase trend
Xenocryst trend
Inherited Argon trend

Figure_12

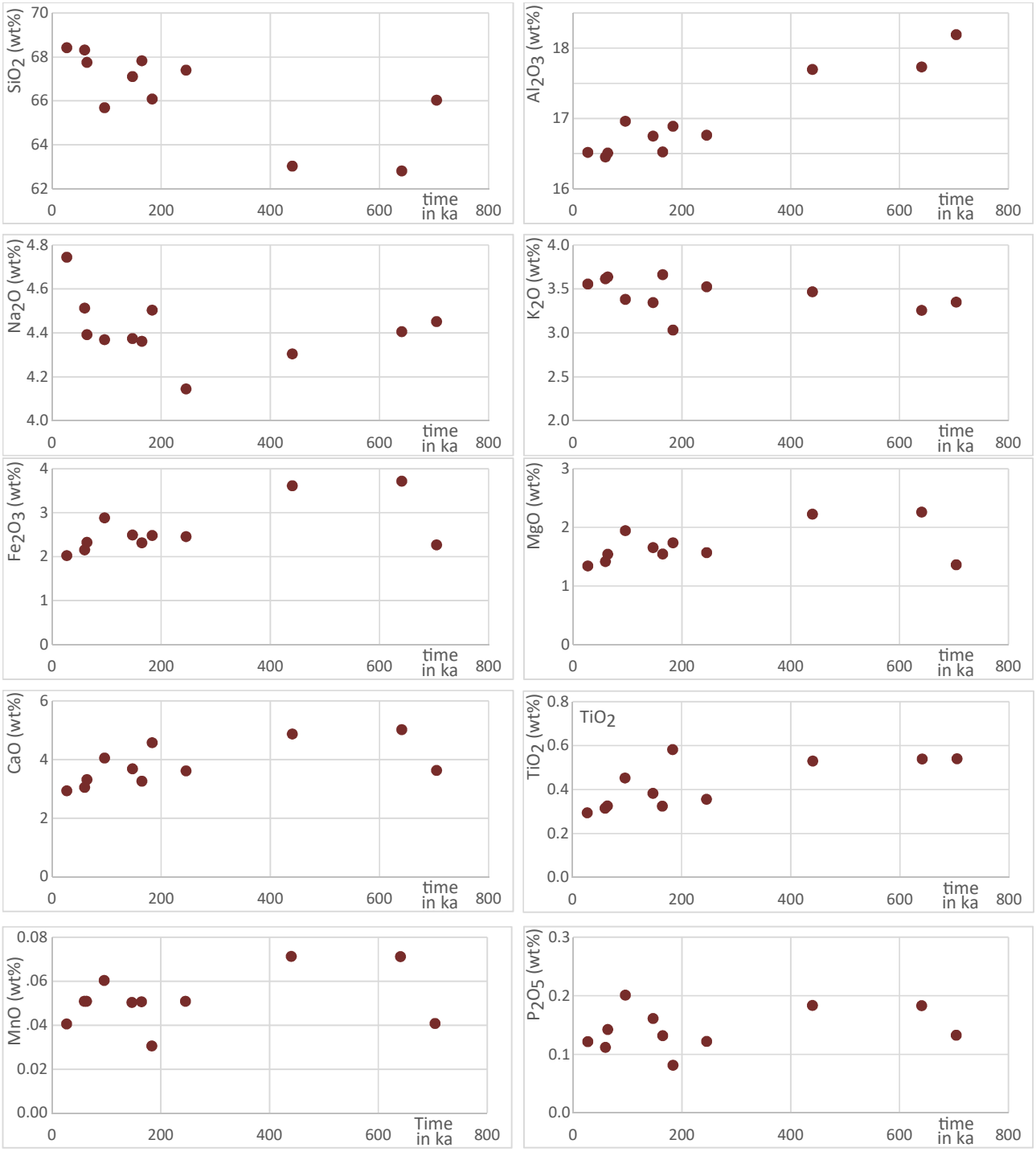
SiO2 (wt%)
70
68
66
64
62
0
200
400
600
800
time in ka
Al2O3 (wt%)
18
17
16
Na2O (wt%)
4.8
4.6
4.4
4.2
4.0
K2O (wt%)
4.0
3.5
3.0
2.5
2.0
Fe2O3 (wt%)
4
3
2
1
0
MgO (wt%)
3
2
1
0
CaO (wt%)
6
4
2
0
TiO2 (wt%)
TiO2
0.8
0.6
0.4
0.2
0.0
MnO (wt%)
0.08
.06
.04
0.02
0.00
Time in ka
P2O5 (wt%)
0.3
0.2
0.1
0.0